AD-A078 516

PANAMETRICS INC WALTHAM MASS
DESIGN, CONSTRUCTION AND TESTING OF A MAGNETIC ELECTRON SPECTRO--ETC(U)
SEP 79   F A HANSER , B SELLERS

F/G 14/2

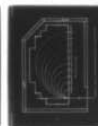F19628-77-C-0180

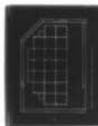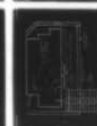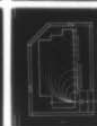UNCLASSIFIED

AFGL-TR-79-0229

NL

I OF I
AD-
A078516

END
DATE
FILMED

1-80

DDC

NATIONAL BUREAU OF STANDARDS
MICROCOPY RESOLUTION TEST CHART

AFGL-TR-79-0229

LEVEL II

DESIGN, CONSTRUCTION AND TESTING OF A MAGNETIC ELECTRON
SPECTROMETER FOR DETECTING ELECTRONS TO 10 MeV, INCLUD-
ING A PRELIMINARY DESIGN FOR A FLIGHT UNIT

Frederick A. Hanser
Bach Sellers

Panametrics, Inc.
221 Crescent Street
Waltham, Massachusetts 02154

September 1979

Final Report

June 1977 - September 1979

D D C

DEC 18 1979

B

AIR FORCE GEOPHYSICS LABORATORY
AIR FORCE SYSTEMS COMMAND
UNITED STATES AIR FORCE
HANSCOM AFB, MASSACHUSETTS 01731

| REPORT DOCUMENTATION PAGE | | READ INSTRUCTIONS BEFORE COMPLETING FORM |
|---|---|---|
| 1. REPORT NUMBER AFGL-TR-79-0229 | 2. GOVT ACCESSION NO. | 3. RECIPIENT'S CATALOG NUMBER |
| 4. TITLE (and Subtitle) Design, Construction and Testing of a Magnetic Electron Spectrometer for Detecting Electrons To 10 MeV, Including a Preliminary Design for a Flight Unit | | 5. TYPE OF REPORT & PERIOD COVERED Final Report June 77 — Sept 79 |
| | | 6. PERFORMING ORG. REPORT NUMBER Final Report |
| 7. AUTHOR(s) Frederick A. Hanser Bach Sellers | | 8. CONTRACT OR GRANT NUMBER(s) F19628-77-C-0180 |
| 9. PERFORMING ORGANIZATION NAME AND ADDRESS Panametrics, Inc. 221 Crescent Street Waltham, MA 02154 | | 10. PROGRAM ELEMENT, PROJECT, TASK AREA & WORK UNIT NUMBERS 62101F 2311G1AF |
| 11. CONTROLLING OFFICE NAME AND ADDRESS Air Force Geophysics Laboratory Hanscom AFB, MA 01731 Contract Monitor: G. Kenneth Yates PHG | | 12. REPORT DATE September 1979 |
| | | 13. NUMBER OF PAGES 67 |
| 14. MONITORING AGENCY NAME & ADDRESS(if different from Controlling Office) | | 15. SECURITY CLASS. (of this report) Unclassified |
| | | 15a. DECLASSIFICATION/DOWNGRADING SCHEDULE |

16. DISTRIBUTION STATEMENT (of this Report)

Approved for public release; distribution unlimited.

17. DISTRIBUTION STATEMENT (of the abstract entered in Block 20, if different from Report)

18. SUPPLEMENTARY NOTES

19. KEY WORDS (Continue on reverse side if necessary and identify by block number)

Electron spectrometer
Magnetic electron spectrometer
Spectrometer

20. ABSTRACT (Continue on reverse side if necessary and identify by block number)

A magnetic electron spectrometer for electrons to 10 MeV energy has been designed, constructed, and tested. The magnet assembly uses rare-earth/cobalt magnets and achieves a gap field of 4 - 4.5 kG. The operation of the spectrometer was tested with beta sources and position sensitive detectors. It was found that a coincidence detector in the entrance collimator eliminates most of the bremsstrahlung background.

DD FORM 1473 EDITION OF 1 NOV 65 IS OBSOLETE
1 JAN 73

20. Abstract (continued)

Some internal baffles are also necessary to reduce scattered electron background. The tests showed that a magnetic spectrometer which can analyze electrons to more than 10 MeV can be readily constructed. A preliminary design for a flight unit magnetic electron spectrometer is given.

# FOREWORD

The work described in this report was carried out under contract to the Air Force Geophysics Laboratory, Hanscom Air Force Base, Massachusetts. The contract monitor was G. Kenneth Yates of the Space Physics Group. During the program Dr. Yates assisted in carrying out some of the electron path calculations in the magnet assembly and in studies of the fringing field effects. The help of Dr. Yates in carrying our this investigation is greatly appreciated.

# TABLE OF CONTENTS

# LIST OF ILLUSTRATIONS

## LIST OF TABLES

# 1. INTRODUCTION

The reliable detection of high energy (1 to 10 MeV) electrons in space has been a difficult undertaking. Electrons scatter considerably in passing through matter and produce bremsstrahlung which can interact to simulate electrons of different energy. Most regions of the earth's magnetosphere which can contain high energy electrons also contain high energy protons, and the electrons become difficult to detect in the presence of the other radiations.

A number of approaches have been used in the past to detect high energy electrons from satellites. One of the first such detectors was a magnet-scintillator combination for 0.05 to 4 MeV electrons, which was used along with a set of absorber-determined threshold detectors for 1 to 5 MeV electrons (Ref. 1.1). The magnet/scintillator combination was used to be able to distinguish electrons from protons, but bremsstrahlung induced background produced most of the counts below 1.5 MeV (Ref. 1.2). The absorber-determined threshold detectors were also sensitive to protons above 10 to 35 MeV and so cannot distinguish 1 to 5 MeV electrons from these higher energy protons.

A 1 to 10 MeV electron spectrometer has been constructed using a $dE/dx$ - scintillator coincidence measurement (Ref. 1.3). This combination is sensitive to high energy protons ( > 70 MeV) and so has limited use in much of the magnetosphere. A magnetic spectrometer for 0.1 to 1 MeV electrons has also been constructed (Ref. 1.4). The magnetic spectrometer used a gap field of about 1 kGauss and so was limited to about 1 MeV electron energy to avoid excessive size and weight. The magnetic spectrometer had no coincidence detector and, therefore, is susceptible to penetrating high energy protons and bremsstrahlung.

A magnetic electron spectrometer for energies up to 2.5 MeV has been flown (Ref. 1.5) as has one for energies up to 3.1 MeV (Ref. 1.6). Both of these magnetic analyzers use 180 degree bending and have no coincidence detector. They are thus susceptible to high energy penetrating protons and to bremsstrahlung background. The magnetic spectrometer in Ref. 1.5 is reported to have low internal bremsstrahlung sensitivity because of extensive baffles, but external bremsstrahlung flux levels can be quite intense, require large amounts of lead (high Z) shielding, and become much more severe at higher electron energies. The magnetic spectrometer in Ref. 1.6 used shielded detectors adjacent to unshielded detectors to measure background. This leads to gaps in the measured spectrum, as well as limiting the measureable electron count rates to a fraction of the background count rates; the actual fraction depending on counting statistics and background uniformity.

Advances in magnetic materials make it now possible to construct magnetic analyzers with much larger gap fields, up to nearly 5 kG. It thus becomes possible to construct an instrument to detect up to 10 MeV electrons,

and which is not much larger than previous designs. There are possible simplifications from using position sensitive detectors; therefore, a thorough investigation of the design of a 1 to 10 MeV magnetic electron spectrometer is desireable.

This report describes the design, construction, and testing of several configurations, for a magnetic electron spectrometer to cover to at least 10 MeV. The results are used to develop a preliminary design of a flight unit.

## 2. THE MAGNET ASSEMBLY

### 2.1 Design and Construction

A general design for an electron magnetic analyzer is shown in Figure 2.1. This design includes a coincidence detector, a sweeping magnet for low energy electrons, and a proton telescope located in a position completely shielded from electrons to at least 10 MeV. The design uses a semi-circular array of magnets on two iron plates, with a completely enclosing outside return yoke.

The actual magnet design for testing purposes is shown in Figure 2.2. This shows the outline of the top and bottom iron plates, the edge pieces which provide support and a magnetic return path, and the actual positions of the Sm-Co magnets. The iron plates and iron edge pieces are made of 1/4 inch thick ingot iron, which is a high permeability, soft iron. Because of the large stresses from the attractive force of the two magnet poles, a set of aluminum support bars is bolted to each plate set (composed of two three-inch wide pieces of 1/4 inch thick ingot iron), as shown in Figure 2.3. The support bars also have screw holes for attachment to a fixture used to bring the two magnet poles together in the final magnet assembly.

The magnet design uses 18 magnets of nominally 1 x 1 x 1/2 inches and one magnet of 1 x 1/2 x 1/2 inches on each pole plate (Figure 2.2). A set of 36 square rare-earth cobalt ceramic magnets of 1 1/16 x 1 1/16 x 1/2 inches was used for the poles. The magnets were first measured for field strength at five (5) positions on each side of the magnet, and sorted into two groups, based on the highest average field strength, for the top and bottom poles. These magnets were then arranged to give the strongest field near the outer edge of the magnet pole, where the highest energy (10 MeV) electrons travel, to ensure that the magnet assembly would analyze to at least 10 MeV.

Placing the magnets onto the pole plates requires considerable care. The magnets are strongly attracted to the iron, and because of their parallel magnetization, adjacent magnets repel each other. The magnets are somewhat brittle, so that a strong blow with a hard object can cause chipping. Each pole is assembled, one magnet at a time, slipped onto the iron plate near the edge to avoid strong shocks. The outer edges of the magnets are held in place by aluminum brackets and stainless steel screws. As the magnets are added to one edge, screws and washers are used to hold them in place against the mutual repulsive forces. The arrangement of the internal screws is shown in Figure 2.2, with all of the outer edges of the magnets being held by aluminum brackets. The magnet arrangement in Figure 2.2 has spaces between the three rows of magnets because of the necessity of using screws to hold the magnets against their mutual repulsion during assembly of the individual poles.

Once the two poles are completed with the magnets, the 1 1/2 inch high iron edge pieces are mounted on one pole. The poles are then bolted, via the aluminum support pieces, to the plates of an assembly rig, as illustrated in Figure 2.4. The pole pieces are bolted in place with the assembly rig taken apart, and the top plate/moveable plate/slide rods component is then placed on top of the bottom plate. The magnet poles are separated by at least five inches during this step,
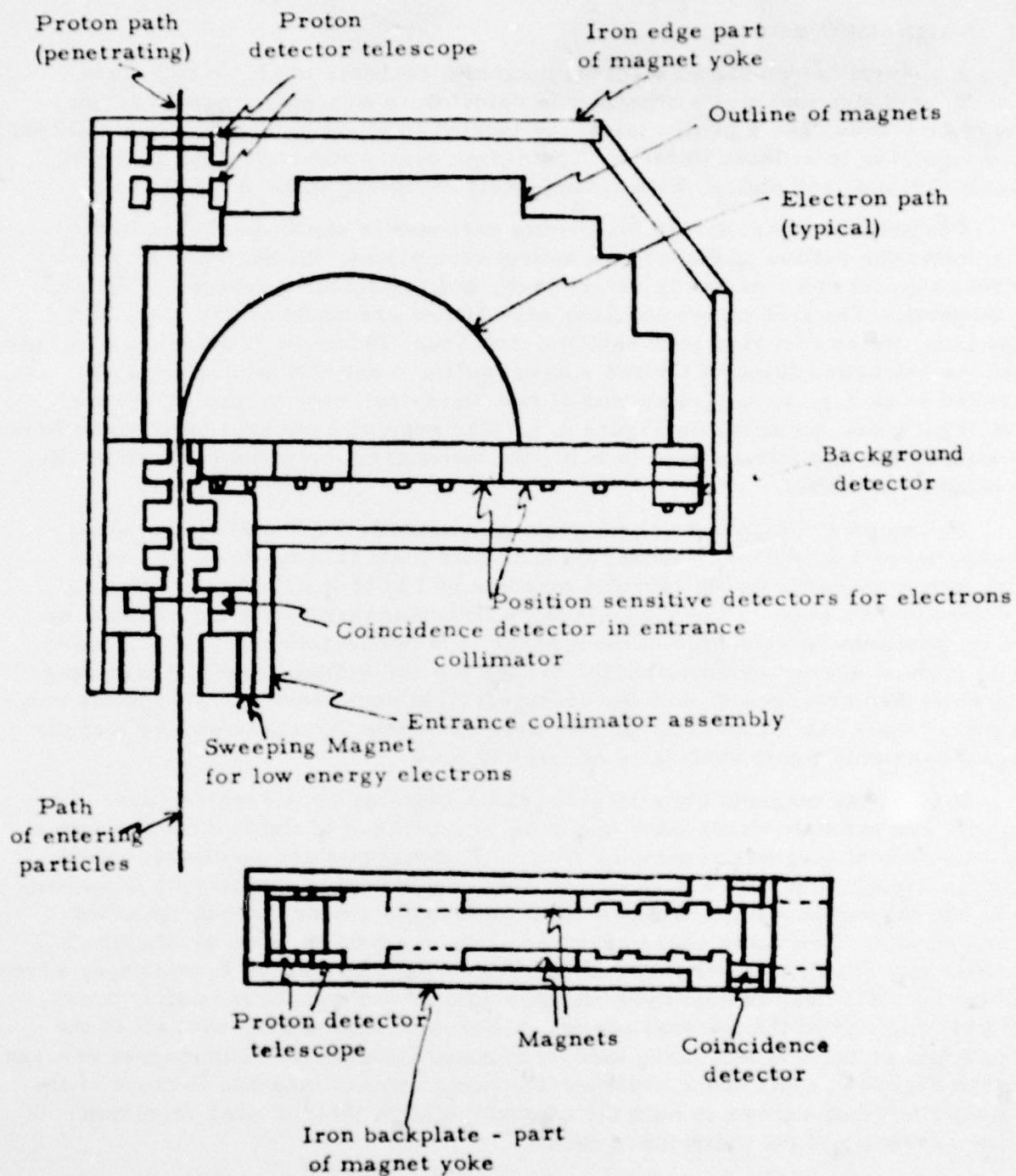
Figure 2.1 General Design of a Magnet Assembly for the Electron
Magnetic Analyzer
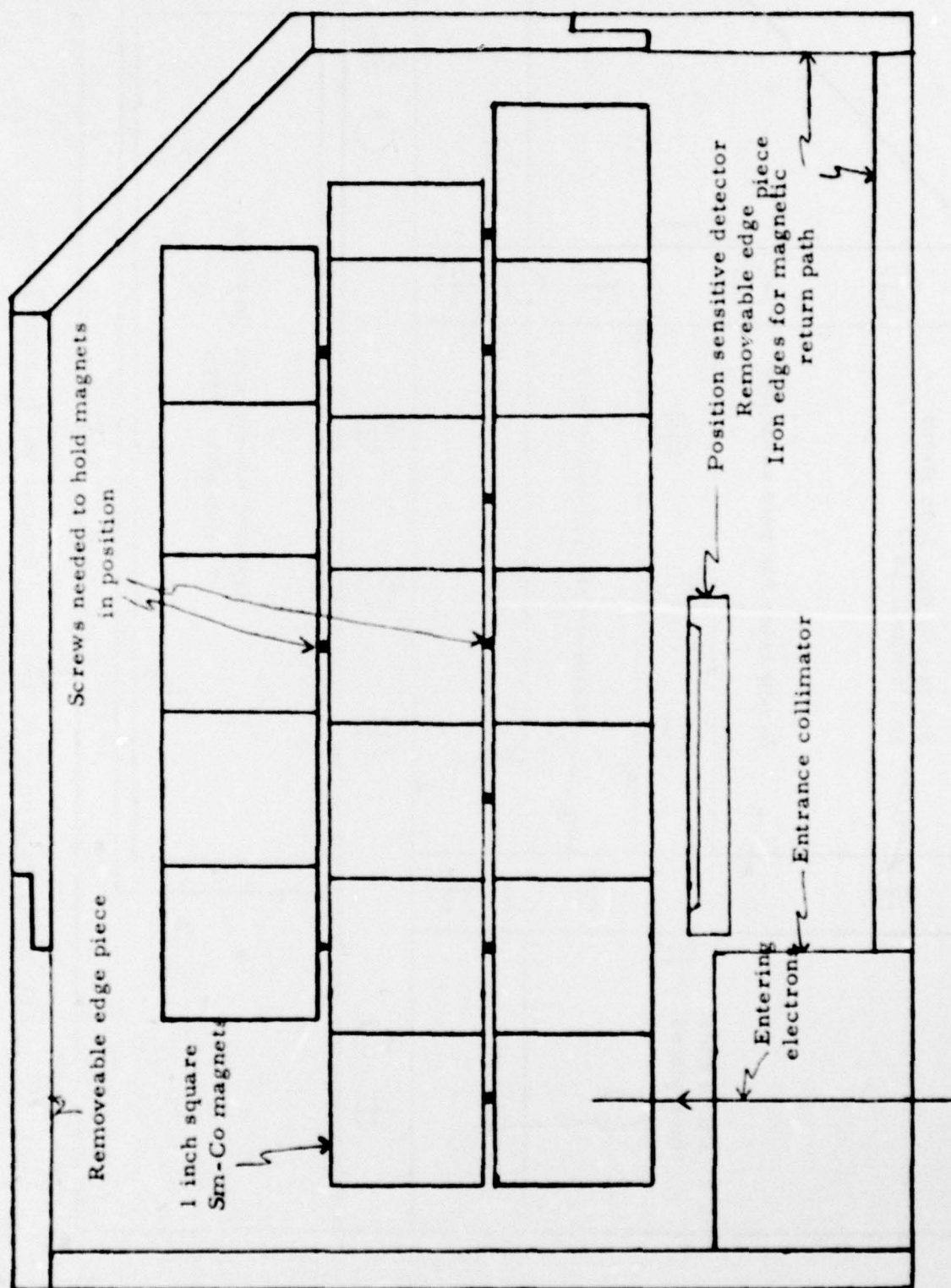
Figure 2.2 Arrangement of Sm-Co Magnets in the Magnet Assembly

Removeable edge piece

Screws needed to hold magnets
in position

1 inch square
Sm-Co magnets

Position sensitive detector
Removeable edge piece
Iron edges for magnetic
return path

Entrance collimator

Entering
electrons
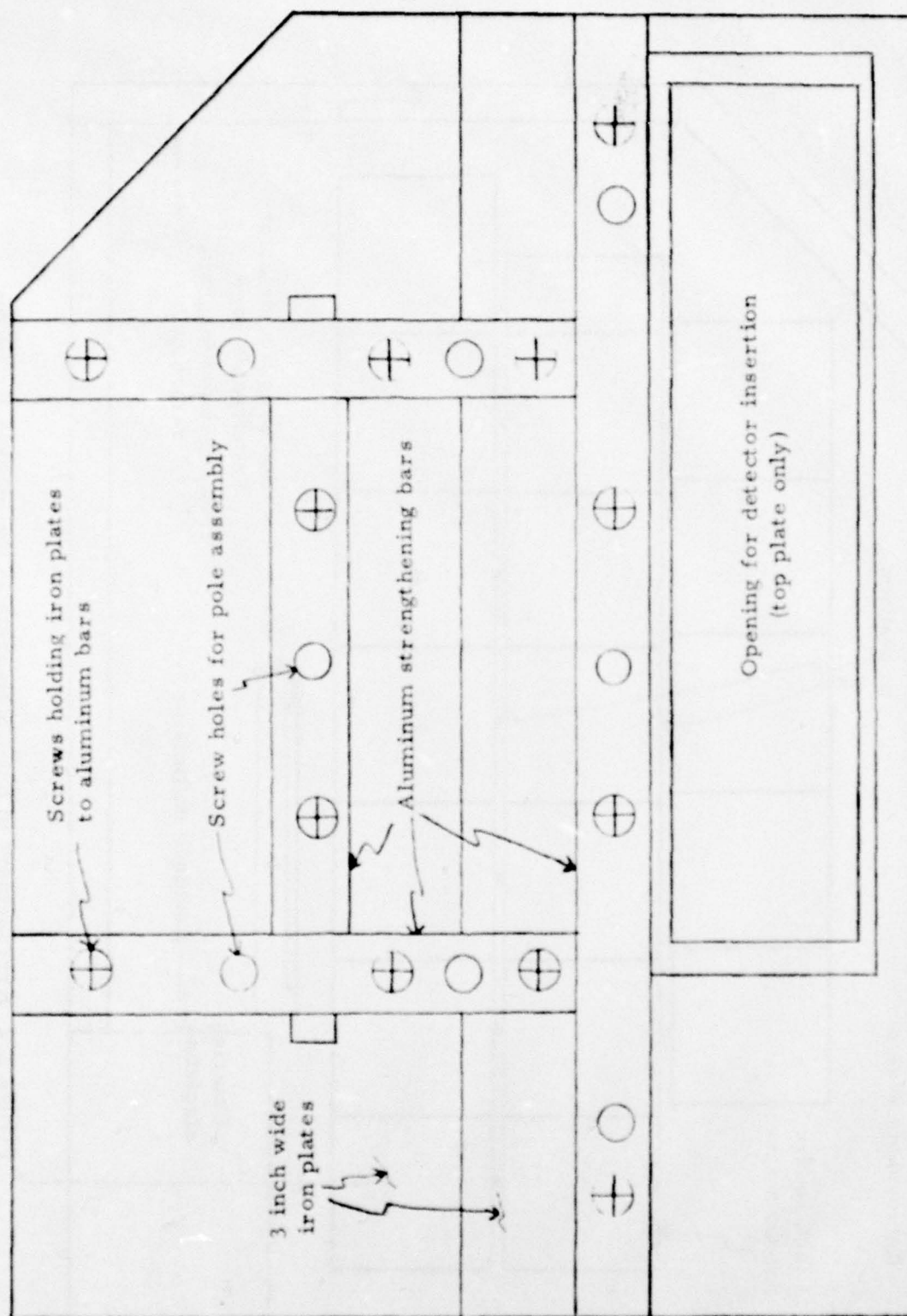
Fig. 2.3 Arrangement of Structural Support and Detector Access Opening for Magnet Poles.

Screws holding iron plates to aluminum bars

Screw holes for pole assembly

Aluminum strengthening bars

3 inch wide iron plates

Opening for detector insertion (top plate only)
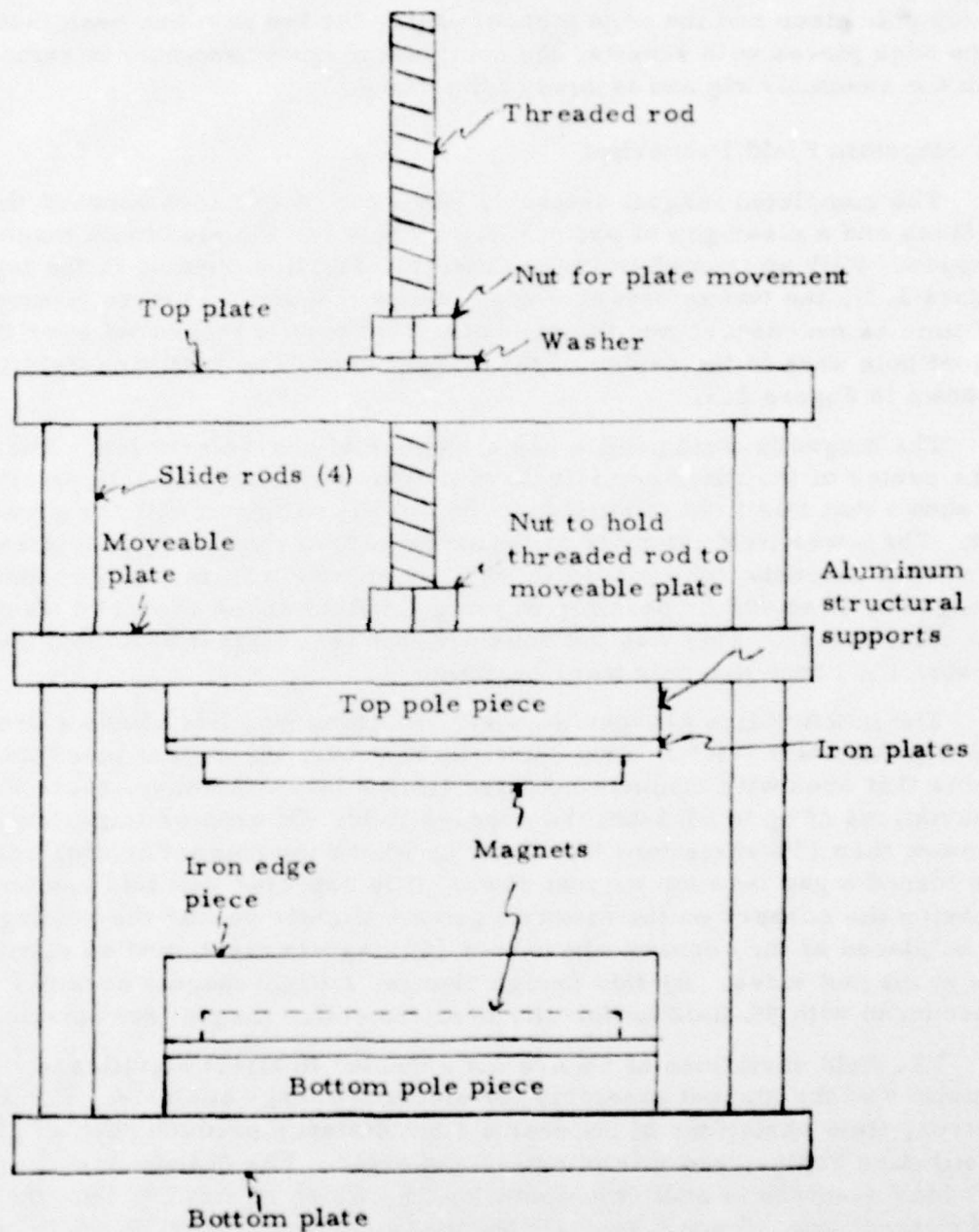
Fig. 2.4. Assembly Rig for Magnet Pole Pieces

since otherwise the magnet poles attract with too much force to allow the operation to be easy and safe. After the bottom plate has been securely fastened, the magnet poles are slowly brought together by turning the nut on the threaded rod. The assembly rig must be rigid and strong, since the magnet poles attract with nearby 1000 lbs. of force just before contact of the top pole piece and the edge pieces. After the top pole has been fastened to the edge pieces with screws, the complete magnet assembly is removed from the assembly rig and is ready for testing.

## 2.2 Magnetic Field Properties

The completed magnet assembly has a gap of 1/2 inch between the magnet faces and a clear gap of about 3/8 inch between the aluminum magnet edge brackets. With an iron plate in the detector insertion opening in the top plate (Figure 2.3), the two removeable edge pieces (Figure 2.2) were taken out one at a time as necessary, and the magnetic field profile measured over the entire magnet pole area in the center of the magnet gap. The resulting field profile is shown in Figure 2.5.

The magnetic field profile has a number of characteristics. The field in the center of the outer semicircle of magnets averages slightly over 4.5 kg and shows that this field intensity can be readily achieved with the present design. The lower field intensity at the inner part of the semicircle is because the weaker magnets were placed there. By selection from a larger number of magnets, it should be possible to bring the field at the center of all magnets to at least 4.5 kg. This was not done with the test magnet assembly because no extra 1 x 1 inch magnets were available.

The junction line between adjacent, touching magnets shows a drop in field intensity of 5 - 10%. This shows up at nearly all magnet junctions and indicates that even with magnets selected from a larger number, there will still be variations of up to 5% from the average field. Of greater importance are the more than 15% variations that show up where the magnet holding screws have forced a gap between magnet rows. It is expected that this can be reduced by having the corners on the magnets ground slightly so that the holding screws can be placed at the corners where four (4) magnets meet, and so eliminate all gaps at magnet sides. By this design change, a flight magnet assembly can be produced with 5% field uniformity over the entire magnet semicircle.

The field variations of 5% are not expected to affect significantly the performances of the magnet assembly for electron energy analysis. For a 5 MeV electron, field variations of 5% over a 1 cm distance produce only a 0.1% change in deflection radius, and this is safely neglected. The change in exit distance for 1 MeV electron is still only about 1 - 2%, which is smaller than the fringing field corrections. Since it is expected that a flight unit would have to be calibrated with electron sources and beams, the field variations of 5% should have no net effect on the performance of a flight instrument.

The field profile along the particle entrance line (the entering electron line of Fig. 2.2 extrapolated straight through the magnet gap) is shown in Figure 2.6.
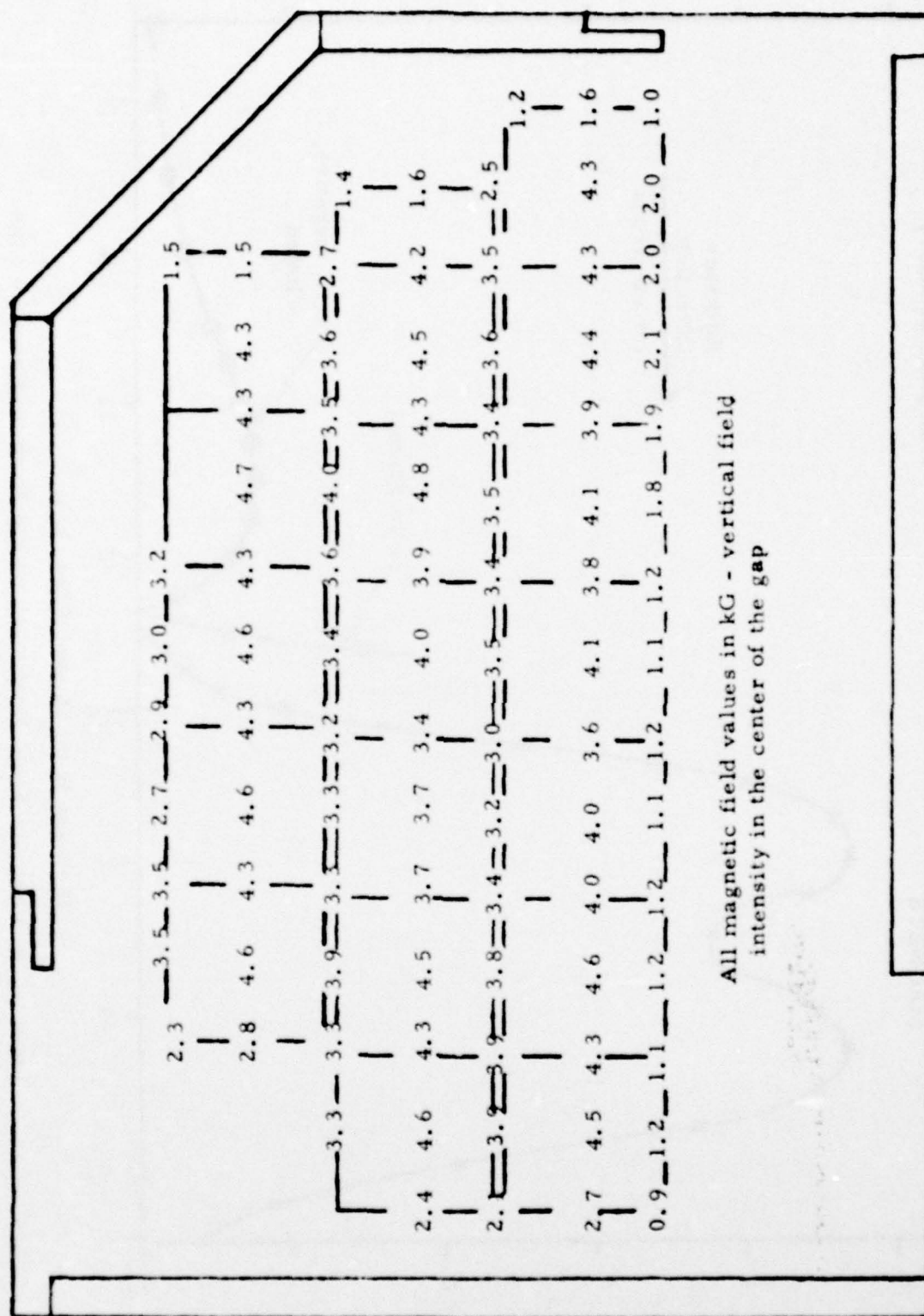
All magnetic field values in kG - vertical field intensity in the center of the gap

Figure 2.5 Measured Magnetic Field Intensities of the Assembled Analyzing Magnet
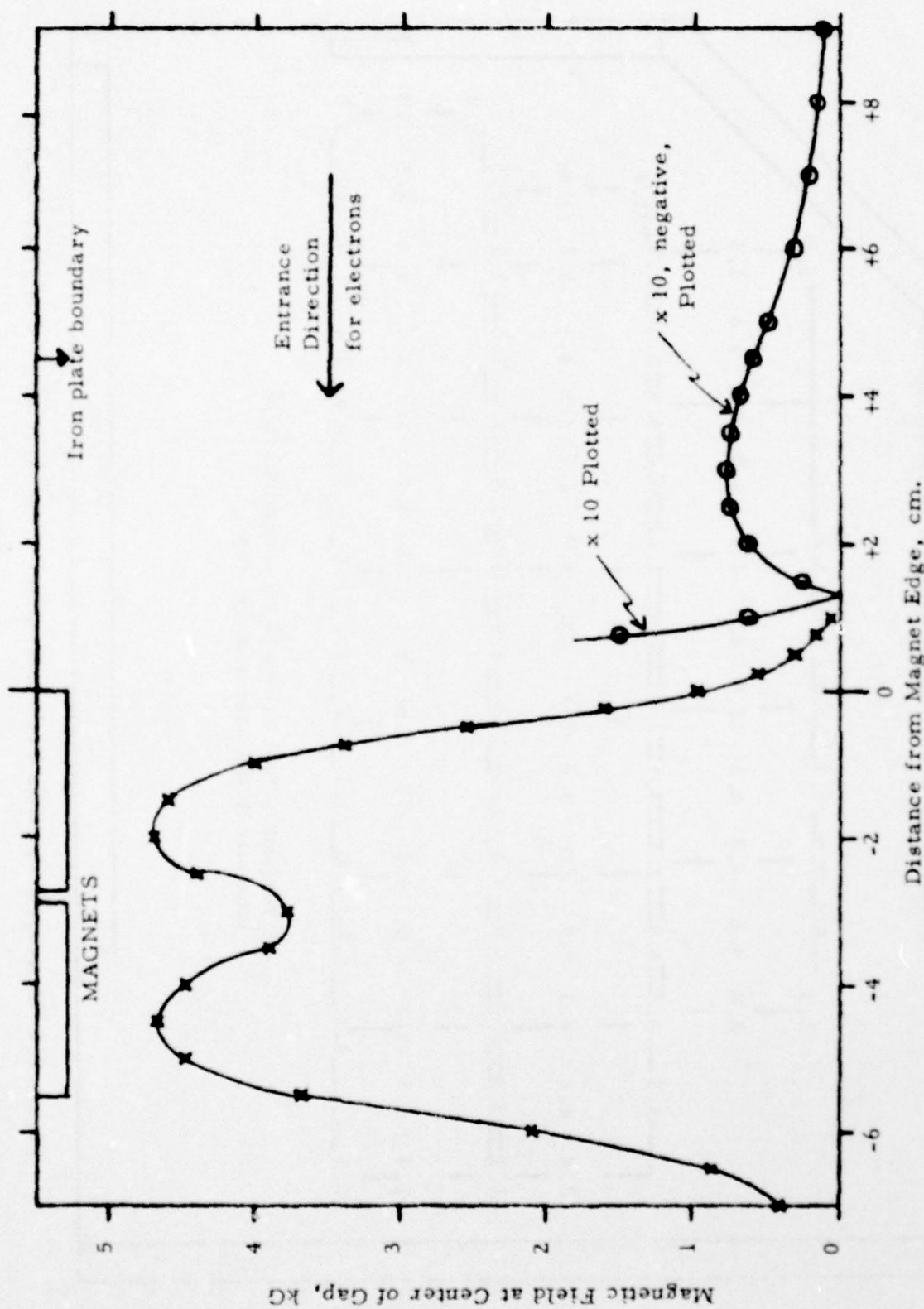
Figure 2.6 Magnetic Field Profile Along the Particle Entrance Line

10

This profile shows the 20% field dip in the 1/16 inch gap between the magnet rows, which should be reduced to about 5% by the magnet modification discussed above. Because of the large (4.5 cm) overhang of the iron pole plates, the fringing field cuts off more sharply and actually reverses direction at about +1.4 cm (0.0 cm coincides approximately with the outer edge of the first magnet). This sharp cut-off and reversal somewhat reduces the fringing field effects on incoming particles.

The measured profile in Figure 2.6 has been fitted to the first maximum at -2.0 cm and used in fringing field calculations. The procedure is discussed in detail in Appendix A. For precise calculations of electron paths in the magnet assembly, both the fringing field effects and the variation of the magnetic field over the pole face (Figure 2.5) must be taken into account. This is particularly true for a flight magnet assembly, where only 5% field variations are expected. For the test magnet assembly, where the field variations are 20% and a lower intensity field occurs near much of the low energy electron exit portion, the major effect on electron paths comes from the internal field variations.

The approximate paths and exit positions for 1 - 10 MeV electrons are shown in Figure 2.7. The electron paths were calculated using the average field intensity along the semicircular part of each path between the magnet poles. The increase in field intensity on the outer semicircular part of the magnet pole results in the spacing change at 6 MeV. As shown, electrons of exactly 10 MeV energy will likely not be analyzed but will escape near the back edge of the pole piece. This results primarily from the reduction in field intensity at the 1/16 inch gaps between magnet rows (Figure 2.2) and should not occur in a flight magnet assembly which does not have these gaps. The addition of a few extra 1 x 1/2 and 1/2 x 1/2 inch magnets would also make the magnet assembly capable of analyzing to at least 10 MeV electrons. The test magnet assembly was only used with beta (electron) sources to 3.5 MeV, so the questionable analysis at 10 MeV is no problem. Since the test magnet assembly definitely analyzes to >9 MeV, the effect of lower energy electron and bremsstrahlung background on the analysis of electrons near 10 MeV can still be investigated.

Figure 2.7 also shows the outline of part of the entrance collimator and the location of the position sensitive detector in the lowest energy position. For this test set-up, the position sensitive detector has a lowest detectable energy of about 1.6 MeV, and a maximum of about 4.4 MeV. All of the testing was done with a Sr-Y-90 beta source of 2.27 MeV maximum electron energy and a Ru-Rh-106 beta source of 3.54 MeV maximum electron energy. Additional details of the test set-up and the results of the testing are given in the following section.

## 3. THE MAGNETIC ELECTRON SPECTROMETER

### 3.1 Spectrometer Assembly for Laboratory Tests

The test magnet assembly described in Section 2 was used with position sensitive detectors, a 200 $\mu$m totally depleted surface barrier detector for coin-

11
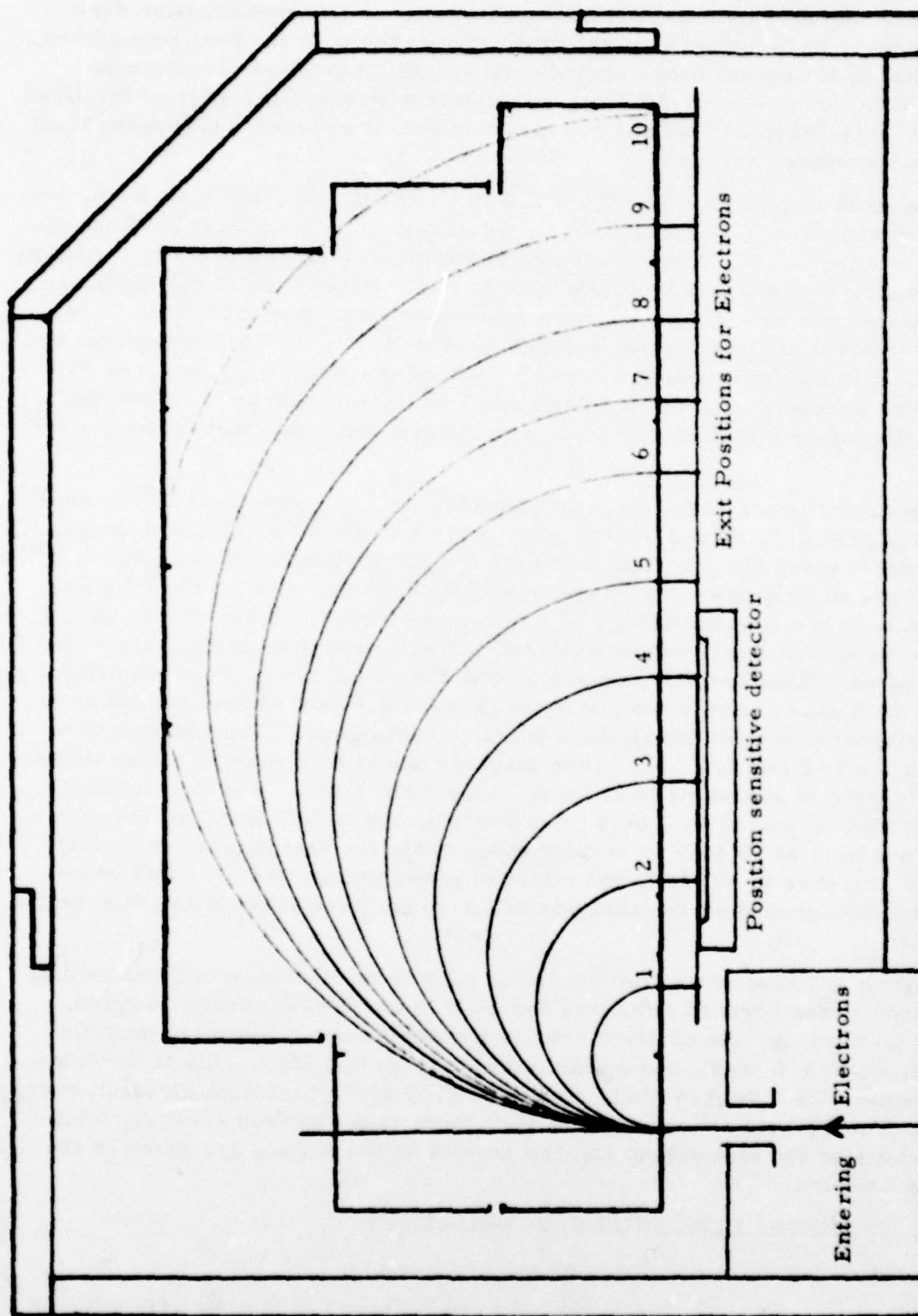
Figure 2.7  Approximate Paths and Exit Positions for 1 - 10 MeV Electrons in the Test
Magnet Assembly

Exit Positions for Electrons

Position sensitive detector

Entering Electrons

1  2  3  4  5  6  7  8  9  10

cidence, a collimator assembly, and internal anti-scattering baffles, as shown in Figure 3.1. The test set-up in Figure 3.1 shows the final config-uration arrived at through many experimental tests with intermediate config-urations. The position sensitive detector (PSD 1) (8 mm x 47 mm sensitive area) was used in any one of the three (3) positions shown, giving a slight overlap between adjacent positions. A second (8 mm x 27 mm) position sen-sitive detector (PSD 2) was also used, both alone and in anticoincidence with PSD 1. When both PSD'S were used, PSD 2 was used only as a detector since only one position sensitive detector analyzer (PSDA) module was available.

A block diagram of the electronics used with the test set-up of Figure 3.1 is shown in Figure 3.2. The complete set-up was not always used, with the 200 μm detector part of the electronics chain and the MCA coincidence input not being used for some of the earlier tests. When PSD 2 was used in anti-coincidence with PSD 1, it was connected in place of the 200 μm detector and the MCA run on anti-coincidence.

3.2 Spectrometer Tests with Radioactive Sources

The experimental configuration for most of the beta source tests with the spectrometer is shown in Figure 3.3. One of the first tests was done with the 8 x 27 mm PSD (PSD 2) used with the PSDA, and positioned to detect 1.5 to 3.2 MeV electrons. The resulting spectra (energy and position) for a Sr-Y-90 beta source are shown in Figure 3.4. The PSD spectrum covers channels 1 to 80 (128 is full scale), so it is clear that electrons are being detected well be-yond the 2.27 MeV end-point of the Sr-Y-90 beta source. The log-counts scale shows that changing the energy threshold for position calculation from 250 to 500 keV lowers the electron count rate at 1.5 - 2 MeV log a factor of 5, while at 3 MeV, it is lowered only a factor of 2 - 3. The high energy counts are a combination of bremsstrahlung background and scattered electrons and have a higher average energy loss than real electrons in the 2 MeV region. These tests were made without the 200 μm detector or the baffles.

The above tests were repeated with the 8 x 47 mm PSD (PSD 1) set to detect 1.7 to 4.5 MeV, and position spectra taken with Sr-Y-90 (2.27 MeV max-imum electron energy) and Ru-Rh-106 (3.54 MeV maximum) source. The re-sults are shown in Figure 3.5, and simply extend the results shown in Figure 3.4. All spectra show counts at energies above the beta source end-point. The Sr-Y-90 spectrum, which peaks at about 0.8 MeV, shows a definite change in slope at the end point, while the Ru-Rh-106 spectrum, which peaks at about 1.25 MeV, shows only a slight slope change at the end-point.

Several tests were made to determine the source of the higher energy pseudo-electron background. The 8 x 27 mm PSD 2 was mounted in a higher energy position, and spectra of PSD 1 was taken both free and in anti-coincidence with PSD 2. No significant changes were observed indicating that electron back-scattering from the PSD to a higher energy position (>2 MeV higher) was not the major source of background. Increasing the collimator opening diameter in front of the source by a factor of 2 changed the position spectrum intensity by a factor of about 4, but did not change the shape. This indicates that much of

13
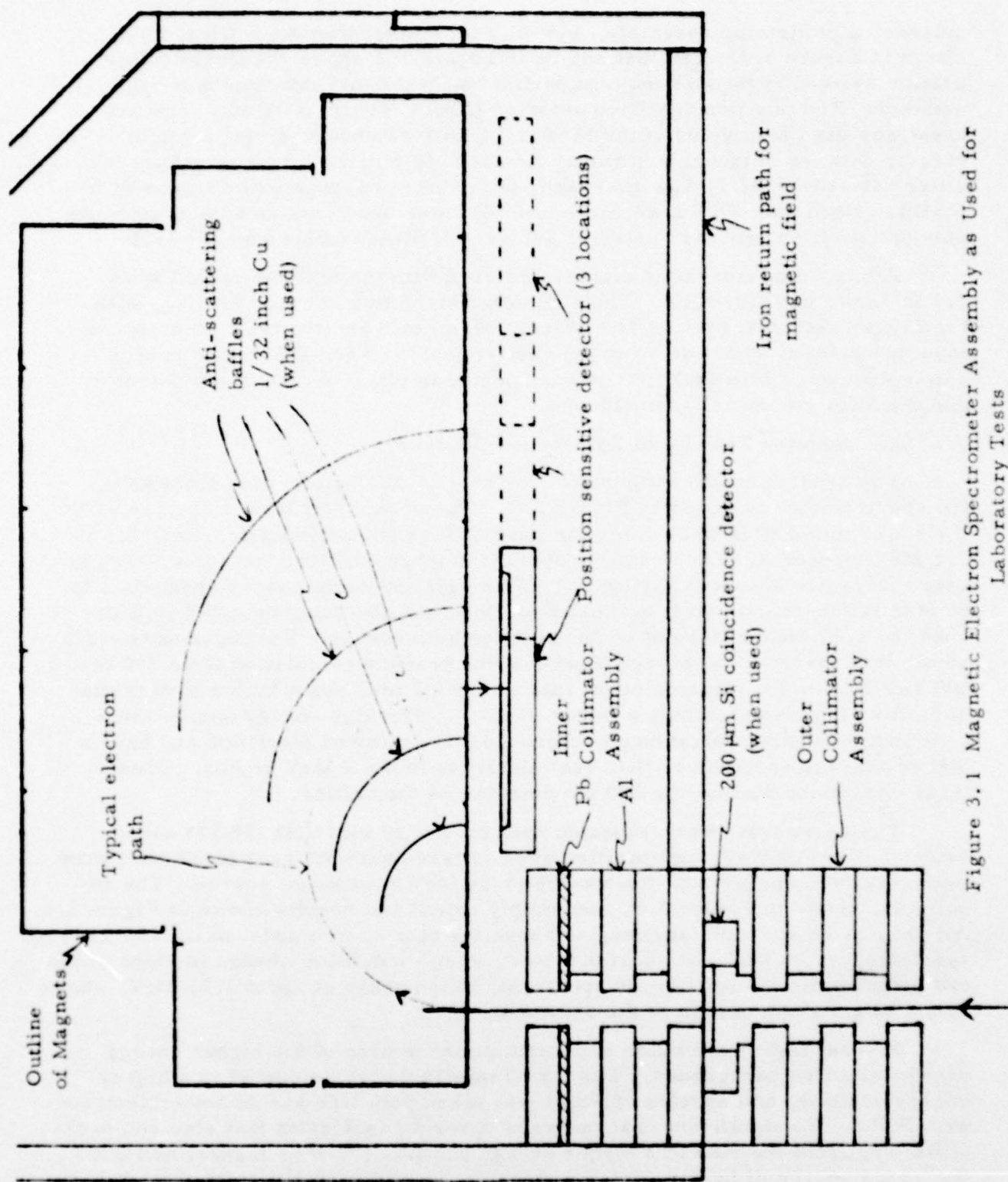
Figure 3.1 Magnetic Electron Spectrometer Assembly as Used for Laboratory Tests

Outline of Magnets

Typical electron path

Anti-scattering baffles 1/32 inch Cu (when used)

Position sensitive detector (3 locations)

Inner Pb Collimator Al Assembly

200 μm Si coincidence detector (when used)

Outer Collimator Assembly

Iron return path for magnetic field

14
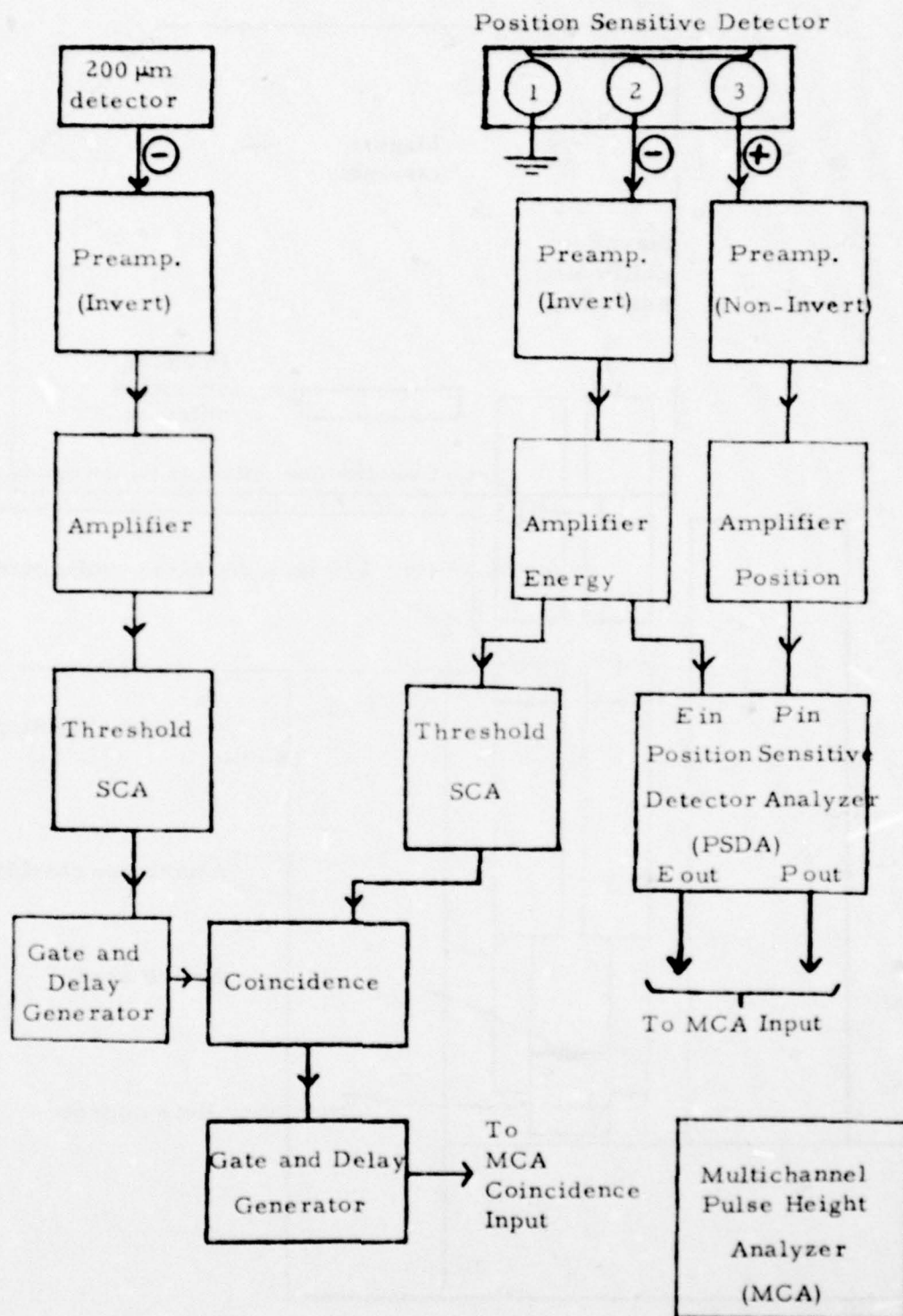
Figure 3.2  Block Diagram of the Electronics Used for Laboratory
Tests of the Magnet Assembly
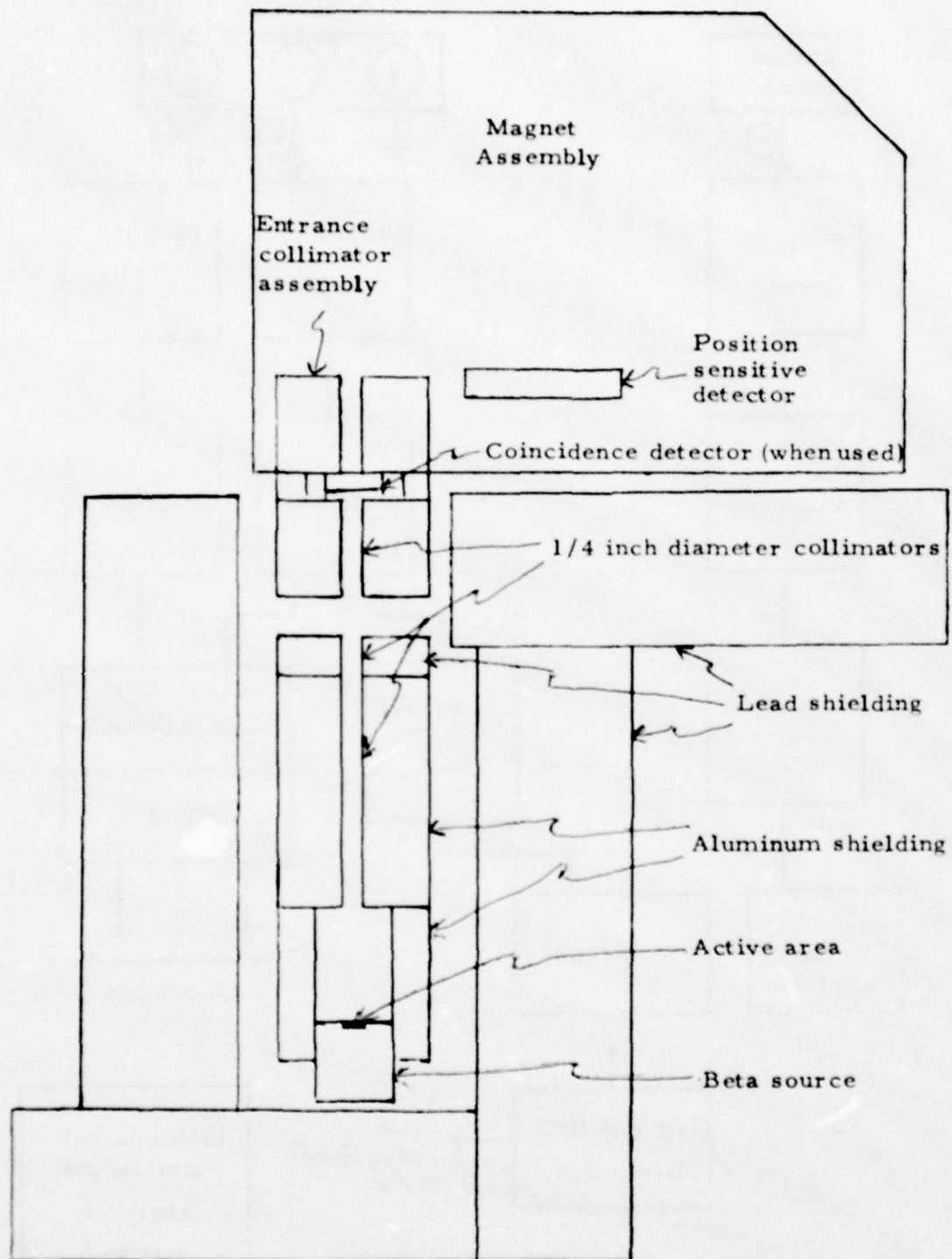
Fig. 3.3. Experimental Configuration for Beta Source Tests.

16

Position Spectra

Log
Counts

Log
Counts

Energy Spectra

Energy
Threshold
=250 keV
(Position
Calculation)

Energy
Threshold
=500 keV
(Position
Calculation)
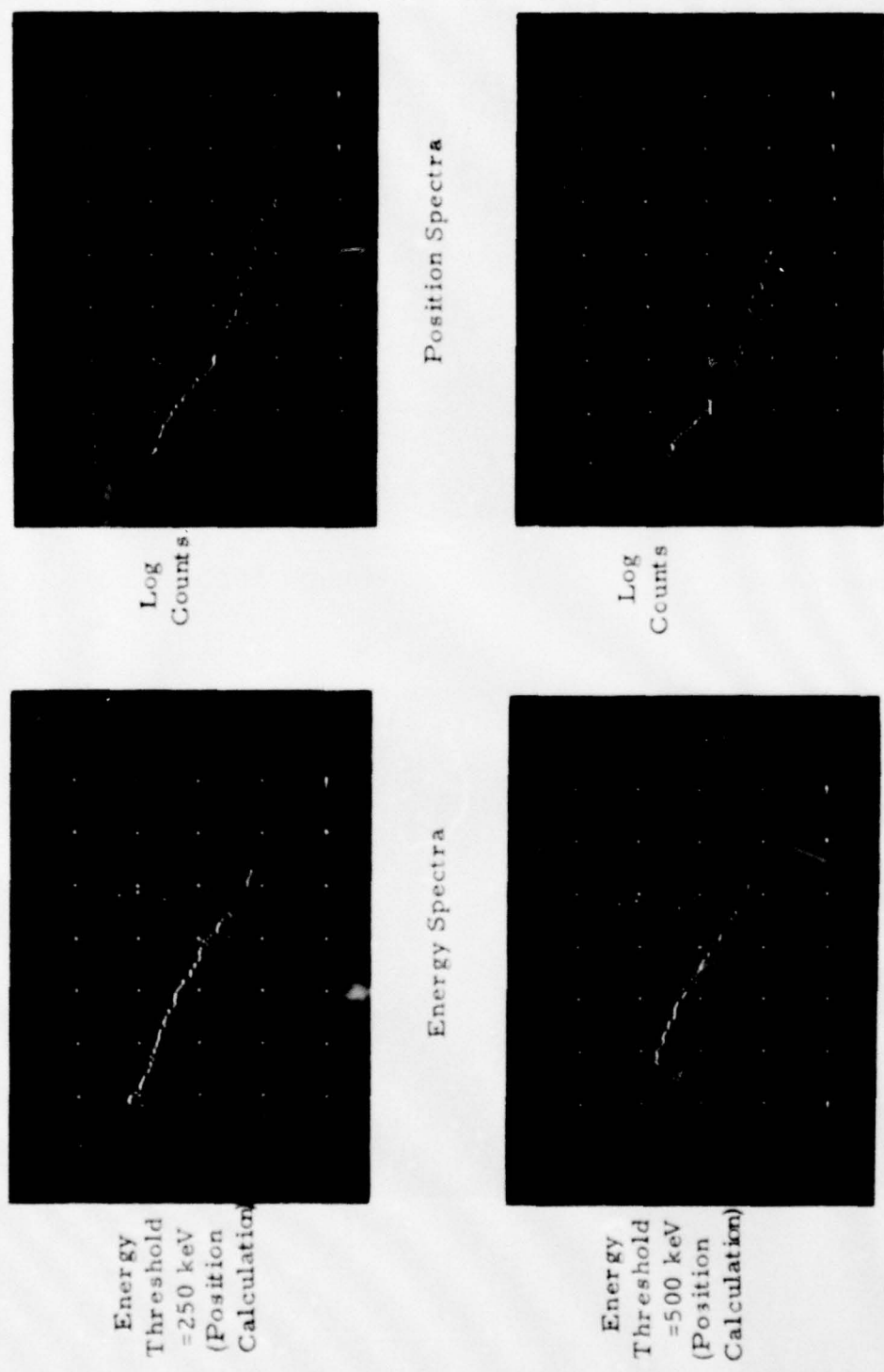
Fig. 3.4. Energy Spectra (left) and Position Spectra (right) for a 10 mCi Sr-Y-90 source, for the approximate position-energy range of 1.5 to 3.2 MeV.

17

Position Spectra

Position Spectra

Log Counts

Log Counts

Energy
Threshold
= 250 keV

(Position
Calculation)

Energy
Threshold
= 500 keV

(Position
Calculation)

Sr-Y-90 (2.27 MeV max.)

Ru-Rh-106 (3.54 MeV max.)
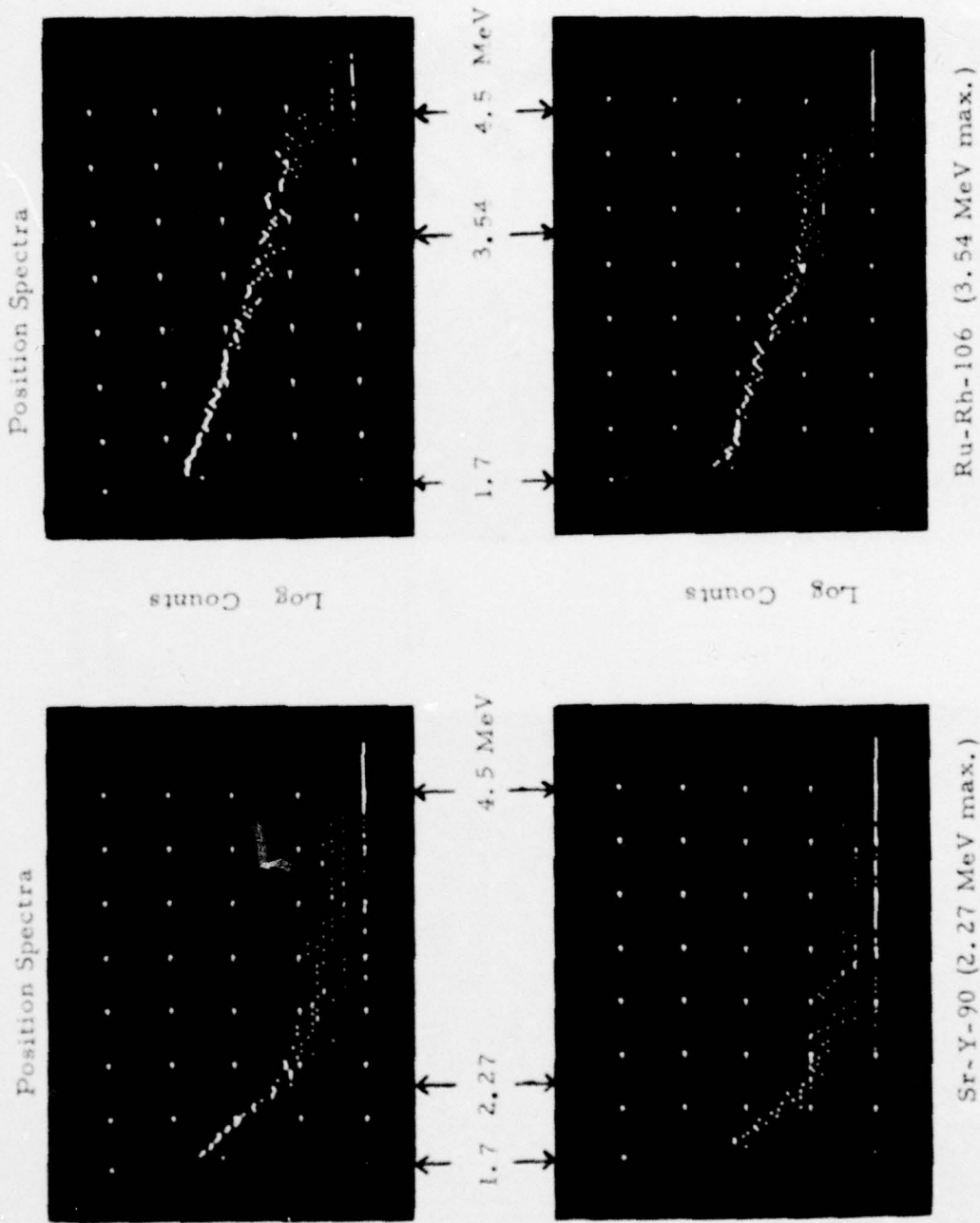
Condition - no 200 μm detector, no anti-scattering baffles

Figure 3.5  Position Spectra for Sr-Y-90 (10mCi  and Ru-Rh-106 (2.5mCi  Beta Sources.

18

the high energy background is associated with the entering electron flux and less with the external bremsstrahlung background.

A set of six (6) anti-scattering strips were placed against each of the magnet poles. The strips were 1/16 inch thick and 1/8 inch wide, made of aluminum, and placed in a fan arrangement radiating from slightly behind PSD 1. These gave no measureable change in the position spectra, and so were not effective in reducing electron scattering and bremsstrahlung production.

A complete set of position spectra for the Sr-Y-90 and Ru-Rh-106 sources is shown in Figure 3.6. The background appears to be composed of two components. A uniform background, evident above 4 - 5 MeV, is most likely due to internal and external bremsstrahlung and is very difficult to shield without using large masses of lead. The other background component appears to be from electrons scattered in the magnet assembly and is most noticeable in the 1 MeV region above the beta spectrum end-point. The spectra in Figure 3.6 were taken with a threshold in the energy pulse of 125 keV. The energy spectra for the 1.6 - 4.4 MeV position of PSD 1 are shown in Figure 3.7, with the Sr-Y-90 results being shown for both free and in anti-coincidence with PSD 2 in a higher energy position, and the Ru-Rh-106 results being shown only for the anti-coincidence. The lack of change in free/anti-coincidence spectra is in agreement with earlier results and conclusions that electrons backscattered from the PSD to a higher energy position (>2 MeV higher) are not an important source of background. It should be noted that the MCA channel for "0" volts input was different for the data in Figures 3.6 and 3.7 ("0" V = Channel No. 10) than for the earlier data in Figures 3.4 and 3.5 ("0" V = Channel No. 0), and this accounts for the peaking at the lowest position signal in Figure 3.6.

The energy spectra in Figure 3.7 show a broad peak at 280 keV, which is the approximate position of the most probable energy loss. The average energy loss is about 360 keV for 1,000 μm of Si and 1-2 MeV electrons. The difference is due to the large amount of straggling in the electron energy loss and is discussed in more detail in Section 3.3.

Electron anti-scattering baffles were installed as shown in Figure 3.1, and position spectra taken with PSD 1. The complete position spectra are shown in Figure 3.8. Comparison with Figure 3.7 shows that the baffles do not affect the counts in the region of beta source electrons, except for the slight dip in the Ru-Rh-106 Position 1 spectrum, which corresponds to a baffle location. The higher energy background is, however, reduced by a factor of 2 to 3 because of the reduction of electron scattering in the magnet gap. There is, however, still an excess of electrons in the 1-2 MeV range just above the beta source end-point energy.

The 200 μm detector was then installed to achieve the full configuration of Figure 3.1. The spectra of the 200 μm detector with the beta sources and a 50 keV threshold are shown in Figure 3.9. The peak occurs at 55 keV and is a partial artifact of the 50 keV threshold. The minimum ionizing energy loss
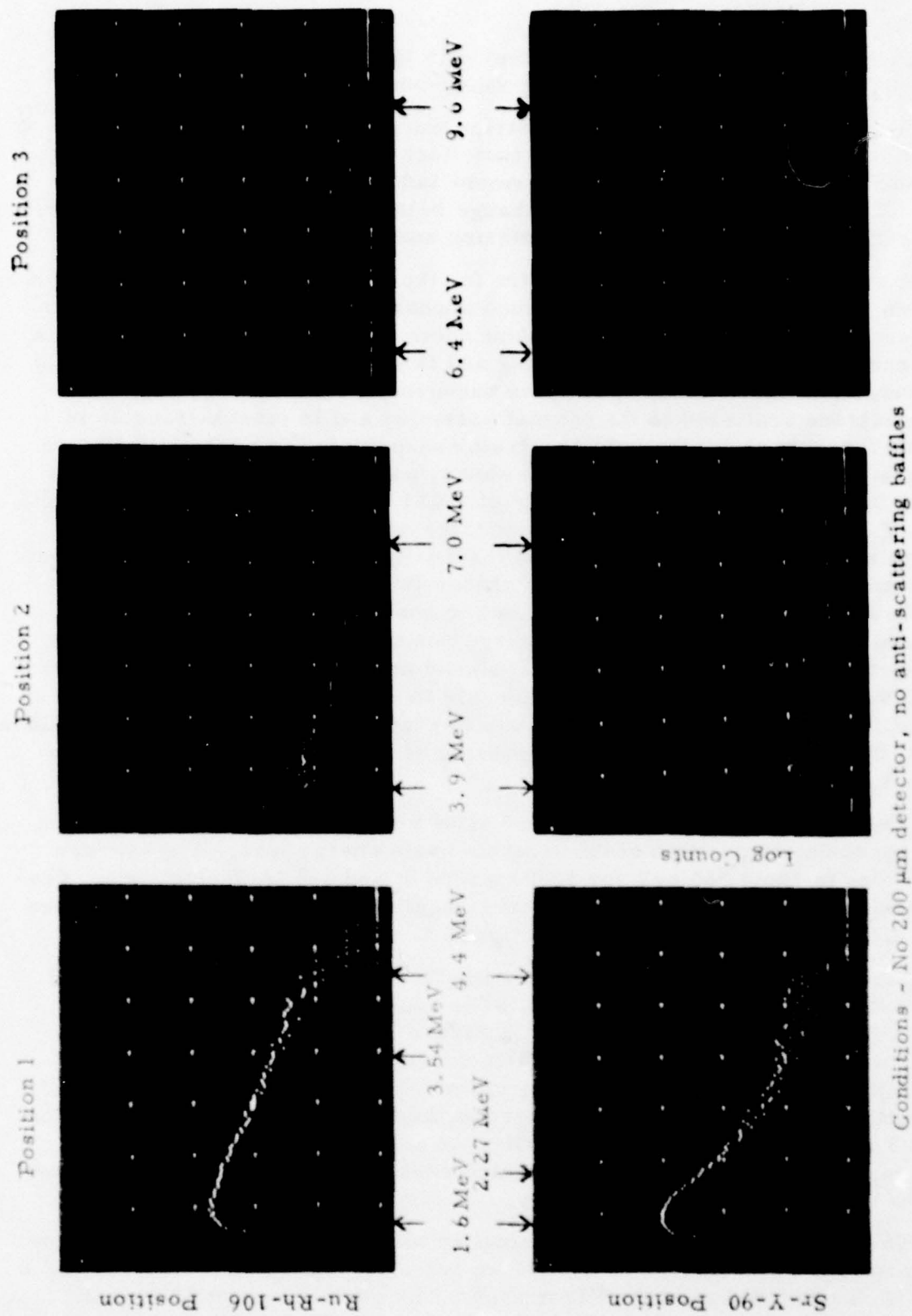
Figure 3.6 Complete Position Spectra for 1.6 to 9.6 MeV, with Beta Sources.

Conditions - No 200 μm detector, no anti-scattering baffles

Position 3

Position 2

Position 1

9.6 MeV

6.4 MeV

7.0 MeV

3.9 MeV

4.4 MeV

3.54 MeV

1.6 MeV

2.27 MeV

Log Counts

Ru-Rh-106 Position
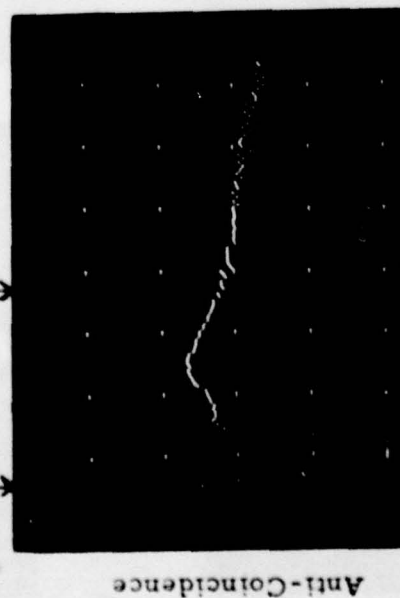
Sr-Y-90 Position

Energy Spectra - threshold = 125 keV

(Position for 1.6 to 4.4 MeV)

Anti-Coincidence is with a higher energy PSD.

Ru-Rh-106

0 keV    500 keV

Anti-Coincidence

Log Counts

Sr-Y-90

500 keV

0 keV

Free

Anti-Coincidence

Figure 3.7 Energy Spectra of the Position Sensitive Detector, for Beta Sources.
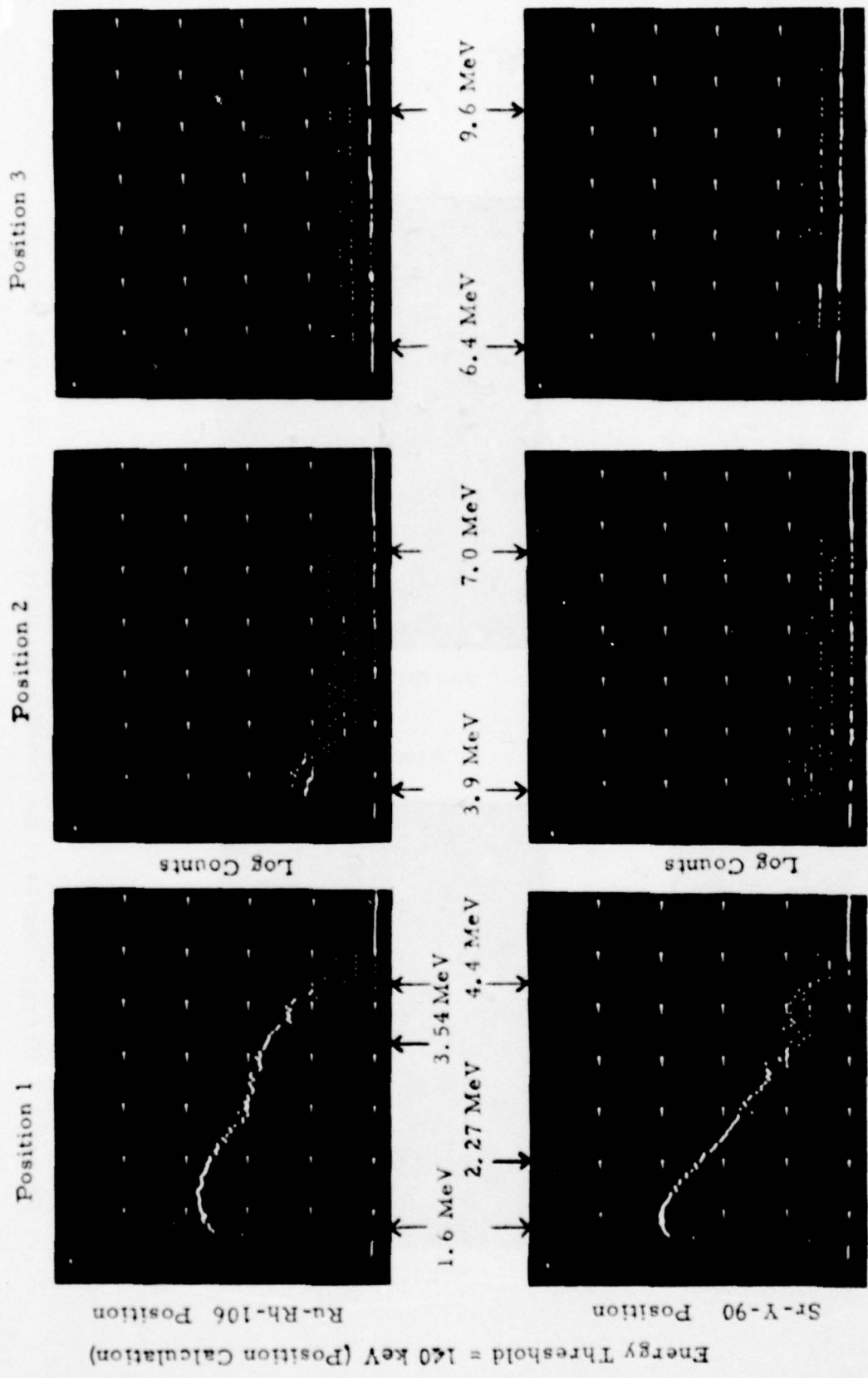
Figure 3.8 Complete Position Spectra for 1.6 to 9.6 MeV, with Beta Sources and Baffles

Conditions - No 200 µm detector, with anti-scattering baffles.

Sr-Y-90

Log Counts

Ru-Rh-106

Log Counts

0 keV          500 keV

Energy Spectra - 200 μm detector

Threshold = 50 keV
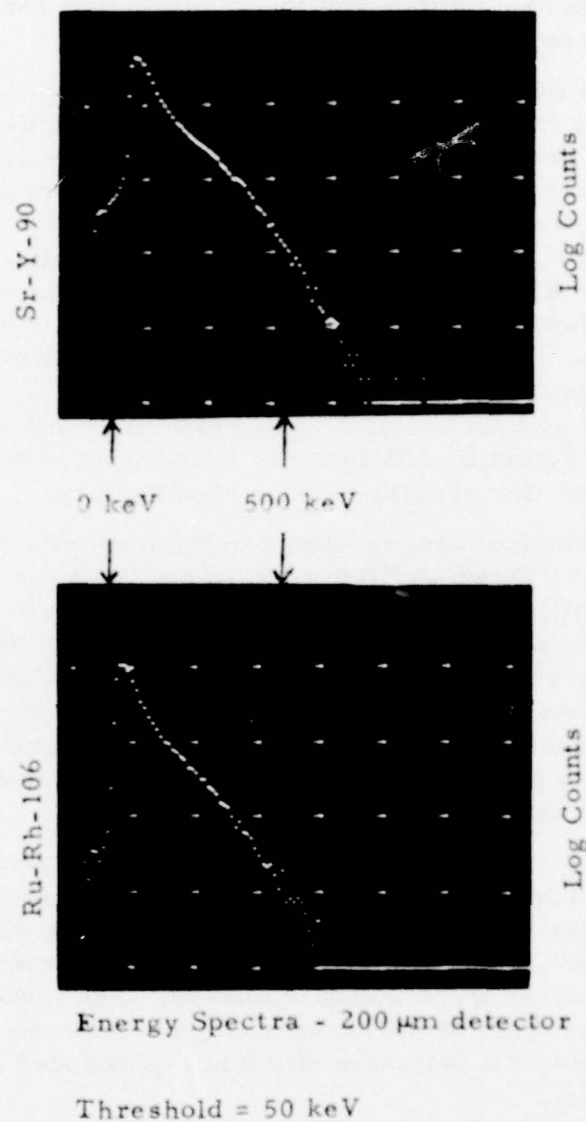
Figure 3.9  Spectra of the 200 μm detector with the Beta Sources.

for 1-2 MeV electrons is about 70 keV, so the most probable energy loss (≃55 keV or slightly less) is significantly lower than the average energy loss. This is in agreement with calculations and the results found for the 1,000 μm thick PSD 1 and is discussed in more detail in Section 3.3.

Spectra of PSD 1 in coincidence with the 200 μm detector with a 50 keV threshold gave extremely low counts, yielding a reduction in detection efficiency by more than two orders of magnitude. To achieve good detection efficiency, it was necessary to lower the 200 μm detector threshold to 15 keV. This was partly into the preamplifier noise, but still yielded a significant improvement in performance. The results for free and coincidence operation of the PSD 1 are shown in Figure 3.10 for the Ru-Rh-106 beta source and in Figure 3.11 for the Sr-Y-90 beta source. These tests were made with the source and two detectors in a straight line, with a small collimator in front of the detectors. The results show that coincidence operation eliminates most of the high energy pulses and the uniform background in position. For the straight line set-up, the detection efficiency is reduced by about a factor of 10, but the energy and position spectra narrow significantly.

The free and coincidence measurements in the magnetic electron spectrometer configuration are shown in Figures 3.12 and 3.13 for the two beta sources. Comparison with the Position 1 results in Figures 3.6 and 3.8 show that the addition of the 200 μm detector reduces the detection efficiency for 1.6 - 2 MeV electrons by about a factor of 4 and coincidence operation by another factor of 3. The overall reduction is thus about a factor of 10. Coincidence operation eliminates most of the spurious counts above the beta source end-point energy. This is particularly shown by the strong reductions at 3.54 MeV in Figure 3.12 and at 2.27 MeV in Figure 3.13.

The coincidence results indicate that much of the background near the beta source end point is due to bremsstrahlung generated in the aluminum electron collimator. Since coincidence requirement with the 200 μm detector eliminates this background, most of it is generated by electrons in the entrance part of the collimator in front of the 200 μm detector. The coincidence requirement thus eliminates most of the background, but because of scattering in the coincidence detector, the detection efficiency is reduced by about a factor of 10.

3.3 Analysis of Spectrometer Response

The geometry for the spectrometer response calculation is shown in Figure 3.14. Since the geometric factor calculation is complex and involves some uncertainty, an actual flight spectrometer must be calibrated with electron beams. For the present case, an approximate calculation is sufficient since it is only necessary to see the effect of various parts of the spectrometer on the geometric factor.

The basic geometric factor is defined by $A_1$, $A_2$, and d, and is given by

$$G_o = A_1 A_2 / d^2 \tag{3.1}$$

24

Figure 3.10  Energy and Position Spectra, Free and Coincidence, for Ru-Rh-106
Beta Source and Straight Line Detection

Position Spectra

Energy Spectra

Log Counts

Log Counts

0 cm     4.6 cm

0 keV     500 keV

Free

Coincidence

(200 μm detector = 15 keV threshold)

Energy threshold (PSD 1) = 125 keV
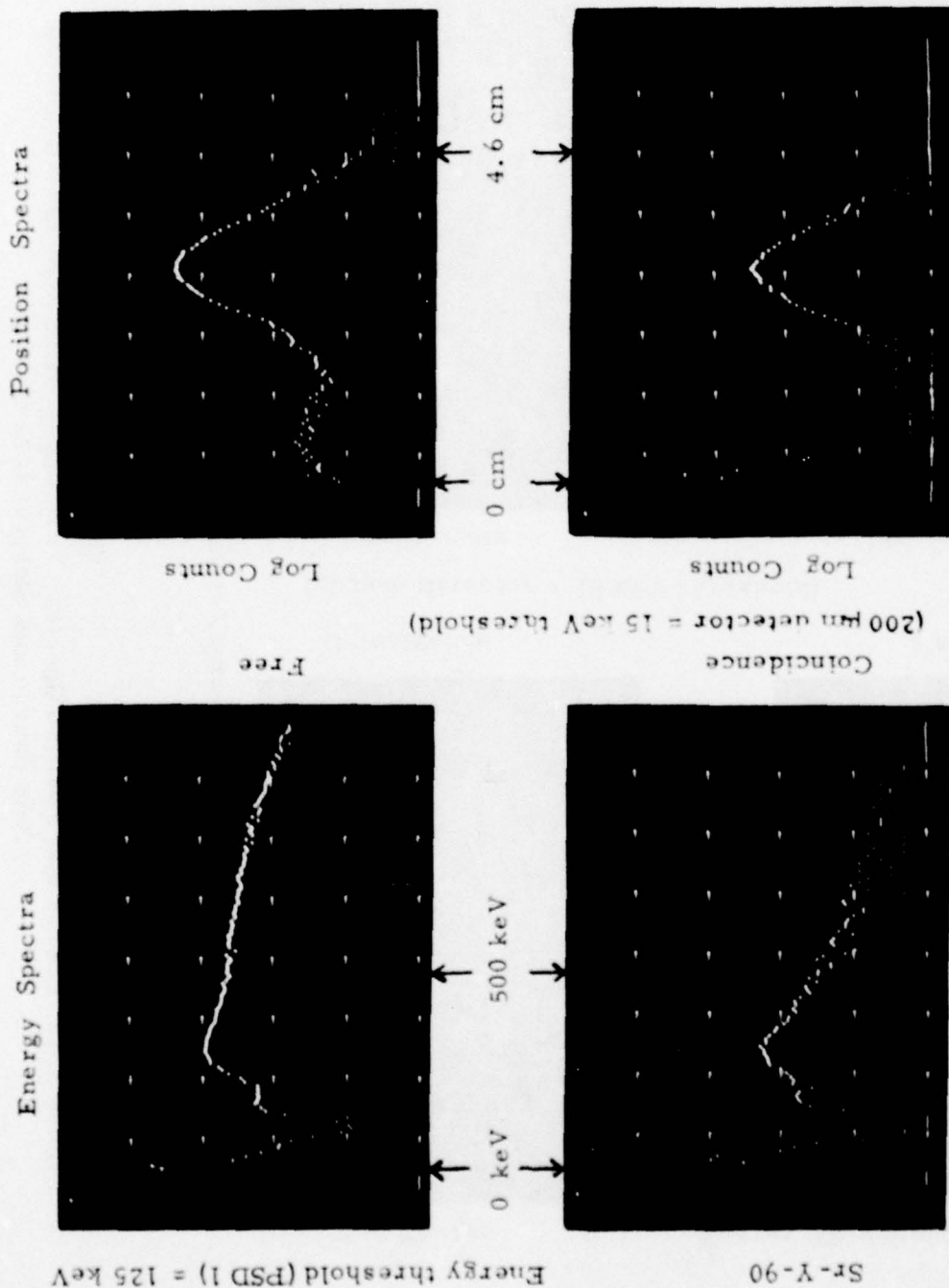
Sr-Y-90

Conditions - With 200 μm detector, straight line detection (no magnet assembly)

Figure 3.11 Energy and Position Spectra, Free and Coincidence, for Sr-Y-90 Beta Source and Straight Line Detection

Position Spectra

Log Counts

Log Counts

4.4 MeV

3.54 MeV

1.6 MeV

Free

Coincidence

(200 µm detector=15 keV threshold)

Energy Spectra

500 keV

0 keV

Energy threshold (PSD I) = 125 keV
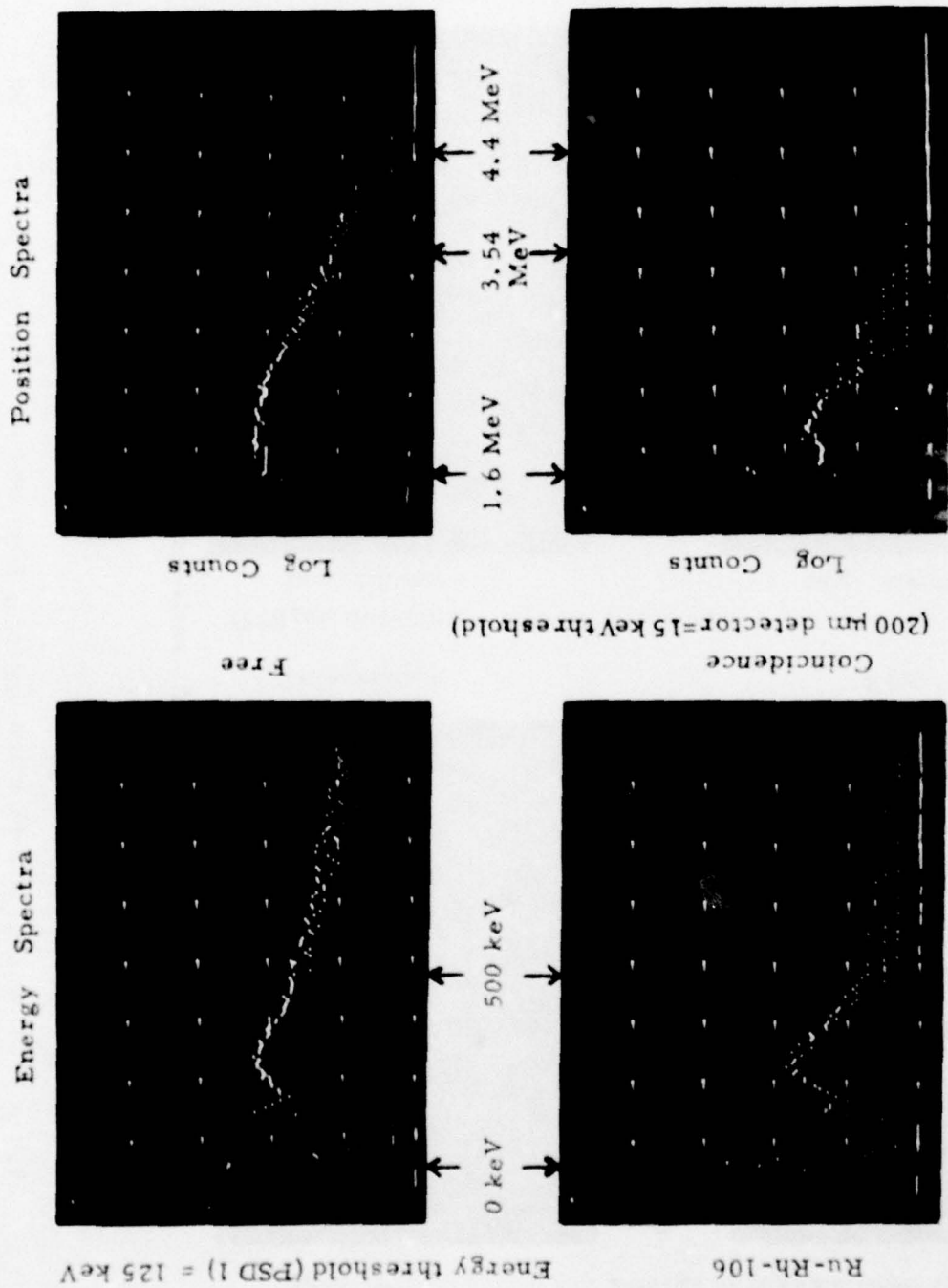
Ru-Rh-106

Conditions - With 200 µm detector, with anti-scattering baffles

Figure 3.12  Energy and Position Spectra, Free and Coincidence, for Ru-Rh-106 Beta Source
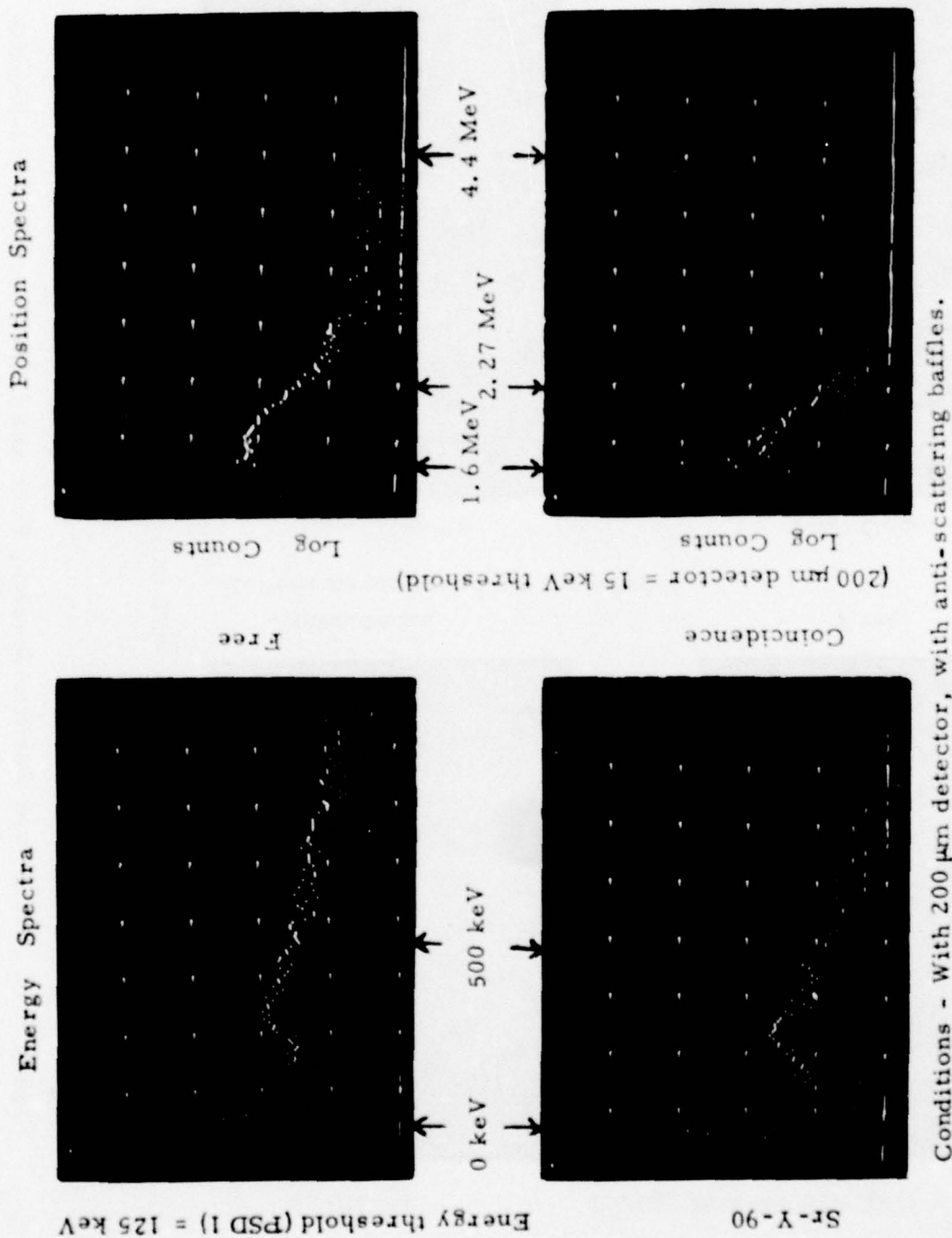
Figure 3.13  Energy and Position Spectra, Free and Coincidence, for Sr-Y-90 Beta Source.

28
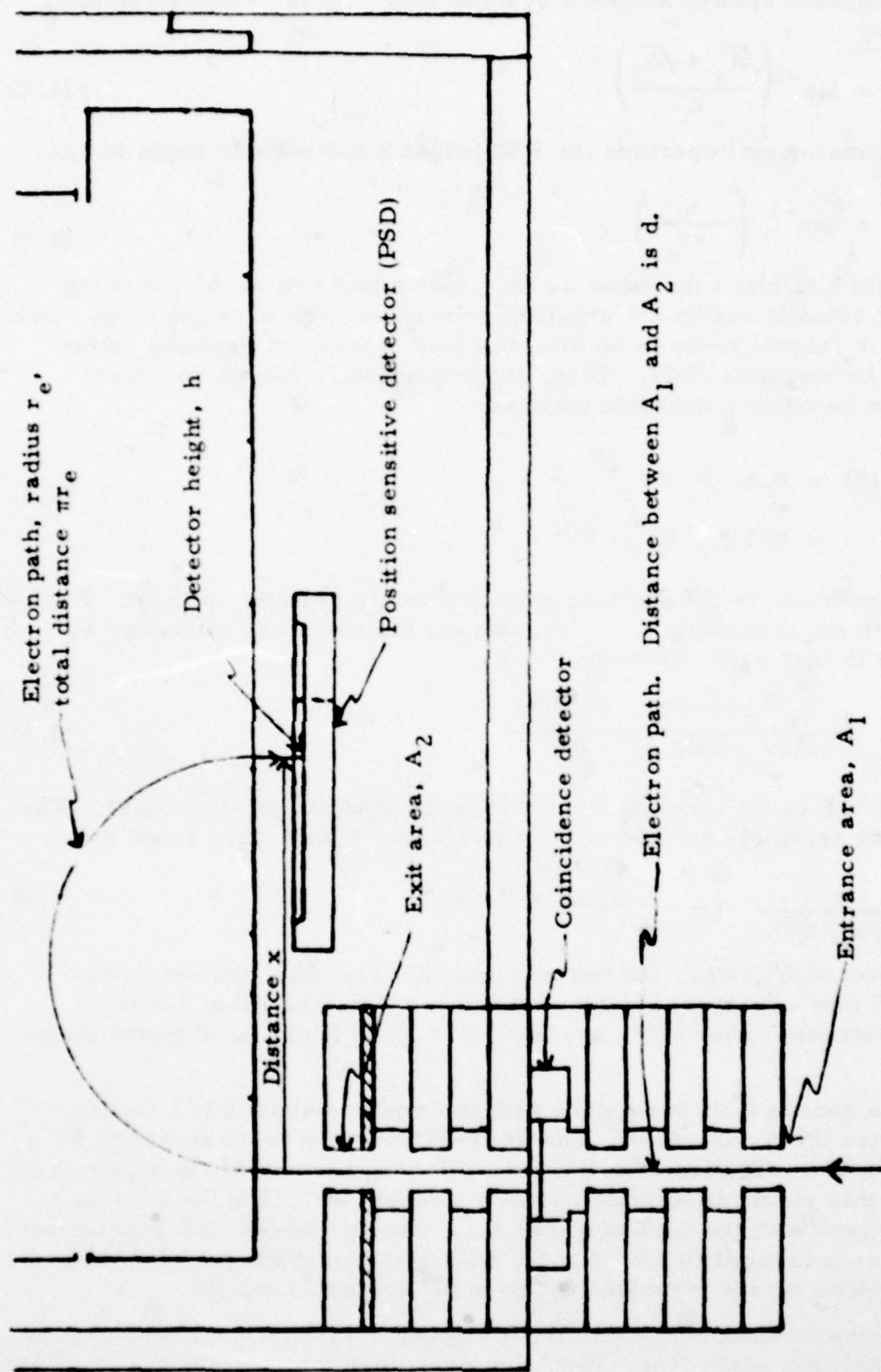
Fig. 3.14. Geometry for Calculation of Spectrometer Geometric Factors.

The input collimator system admits a beam of total angular width given approximately by

$$\theta_o = \tan^{-1}\left(\frac{\sqrt{A_1} + \sqrt{A_2}}{d}\right) \tag{3.2}$$

From the collimator exit aperture the PSD height h subtends an angle of approximately

$$\theta_h = \tan^{-1}\left(\frac{h}{\pi r_e}\right) \tag{3.3}$$

Since the height h is about the same as $\sqrt{A_2}$, only about half of the incoming electrons will actually strike the sensitive part of the PSD even for large values of $\theta_h$. In the $r_e$ plane, there is no electron loss because of focusing by the $180°$ bend in the magnetic field. Thus, the collection factor for electrons leaving $A_2$ can be written approximately as

$$F_o(E) = 0.5, \quad \theta_h \geq \theta_o \tag{3.4}$$
$$= 0.5 \, \theta_h / \theta_o, \quad \theta_h < \theta_o$$

where the dependence on the electron energy E is via $r_e$ in $\theta_h$ in (3.3). For a strip of width $\Delta x$ at position $x = 2r_e$, and for the electrons of energy E, the count rate is then approximately

$$\Delta C = \frac{G_o F_o(E) \Delta x}{2(dr_e/dE)} \frac{d J_e(E)}{dE} \tag{3.5}$$

where $d J_e(E)/dE$ is the incident electron flux in $el/(cm^2\text{-sr-sec-MeV})$. For the test magnet assembly and electrons above about 1 MeV, it is found that

$$\frac{1}{2(dr_e/dE)} \simeq 0.60 \text{ MeV/cm} \tag{3.6}$$

Using the values of $A_1$, etc., for the test magnet assembly, the resulting values of $G\Delta E$ $(cm^2\text{-sr-MeV})$ for $\Delta x = 1$ cm are listed in Table 3.1 for 1 to 10 MeV electrons. The values are for $\Delta E = 0.60$ MeV, as obtained from (3.6).

The beta source tests were done with the sources about 8 1/2 inches (21.59 cm) from the $A_2$ aperture. The Sr-Y-90 source was measured to be 10 mCi, with a 3/8 inch diameter aperture. Taking account of the difference in geometry, this yields an effective source strength of $1.12 \times 10^7$ $el/(cm^2\text{-sec-sr})$ to be used with the $G\Delta E$ of Table 3.1. For the Ru-Rh-106 beta source, the activity was measured to be 2.5 mCi, with a source diameter of 3/16 inch, giving an effective source strength of $2.80 \times 10^6$ $el/(cm^2\text{-sec-sr})$.

Source measurements made in the air require an additional consideration for electron multiple scattering. Electron multiple scattering and the resulting

30

## TABLE 3.1

### Geometric Factors for Test Magnet Assembly

| Electron Energy (MeV) | $x = 2r_e$ (cm) | $\theta_h$ (deg) | $F_o$ (E) | $G\Delta E \ (\Delta x = 1 \text{ cm})^*$ $= 2 G_o F_o \Delta E$ $(\text{cm}^2\text{-sr-MeV})$ |
|---|---|---|---|---|
| 1 | 2.4 | 11.98 | 0.50 | $5.37 \times 10^{-4}$ |
| 2 | 4.2 | 6.91 | 0.40 | $4.30 \times 10^{-4}$ |
| 3 | 5.8 | 5.02 | 0.29 | $3.11 \times 10^{-4}$ |
| 4 | 7.6 | 3.83 | 0.22 | $2.36 \times 10^{-4}$ |
| 5 | 9.2 | 3.17 | 0.19 | $2.04 \times 10^{-4}$ |
| 6 | 11.0 | 2.65 | 0.16 | $1.72 \times 10^{-4}$ |
| 7 | 12.2 | 2.39 | 0.14 | $1.50 \times 10^{-4}$ |
| 8 | 13.6 | 2.14 | 0.13 | $1.40 \times 10^{-4}$ |
| 9 | 15.2 | 1.92 | 0.11 | $1.18 \times 10^{-4}$ |
| 10 | 17.0 | 1.72 | 0.10 | $1.07 \times 10^{-4}$ |

\* Parameters for $A_1 = A_2 = 0.317 \text{ cm}^2$, d = 7.5 cm, h = 0.8

For $\Delta x$ = 1 cm, $\Delta E$ = 0.60 MeV, nearly constant for 1 - 10 MeV.

angular and radial distributions are treated in Ref. 3.1, pp. 282 - 292. For electrons penetrating a thickness $t(g/cm^2)$ of material Z, A(atomic number and weight), the probability distribution in angle is

$$P(\theta)\, d\theta = \frac{2}{\langle \theta^2 \rangle} \theta e^{-\theta^2/\langle \theta^2 \rangle} d\theta \qquad (3.7)$$

where

$$\langle \theta^2 \rangle = \frac{0.157 Z(Z+1) t}{(pv)^2 A} \text{ In } \frac{1.13 \times 10^4 Z^{4/3} t}{(v/C)^2 A} \qquad (3.8)$$

with v the electron velocity, c the velocity of light and p the electron momentum with (pv) in MeV. The lateral displacement distribution after traveling y cm, which contains the t g/cm$^2$ of material, is

$$F(r, y)\, dr = \frac{6r\, dr}{\langle \theta^2 \rangle y^2} e^{-3r^2/(\langle \theta^2 \rangle y^2)} \qquad (3.9)$$

where $\langle \theta^2 \rangle$ is calculated for t with (3.8).

31

The above distributions must be used twice, once for the path from the beta source to $A_2$, and once from $A_2$ to the PSD. For the first path, the parameters are $\bar{y} = 21.59$ cm, $t = 0.0259$ g/cm$^2$, and $R = 0.318$ cm. The results for $\langle \theta^2 \rangle$ and $P(r \leq R)$ are given in Table 3.2, where $P(r \leq R)$ is obtained from integration of (3.9) and is

$$P(r \leq R) = 1 - e^{-3R^2/(\langle \theta^2 \rangle y^2)} \tag{3.10}$$

For the second path, the calculation is somewhat more complex because to first order the spread in the $r_e$ plane can be neglected, and only those electrons scattered out of this plane and beyond $\pm h/2$ are lost. This can be approximated by taking the square root of (3.10), splitting the circular distribution in half. Doing this gives probabilities ranging from 0.97 at 1.5 MeV to 0.77 at 5.0 MeV, and they are given in the last column of Table 3.2.

The measured position spectra are converted to incident flux by

$$\frac{d J_o(E)}{dE} = \frac{(\text{Measured counts}/\text{channel})}{(\text{cm}/\text{ch}) (\Delta T) (G\Delta E) P(r \leq 0.318) P_1(h)} \tag{3.11}$$

where $G\Delta E$ is taken from Table 3.1, $P$ and $P_1$ from Table 3.2, and (cm/ch) and ($\Delta T$) (count time in seconds) are for the MCA spectrum in question. The spectra in Figure 3.6 have (cm/ch) = 0.063 and ($\Delta T$) = 8 x 60 seconds, with the resulting beta source spectra being given in Table 3.3. The measured spectra are compared to the calculated spectra, based on the Sr-Y-90 and Ru-Rh-106 spectra given in Ref. 3.2. Considering the approximations and corrections made, the agreement is quite good. The dip in (measured/calculated) for Ru-Rh-106 at 2.75 MeV may be due to the dip in magnetic field at the gap between the first and second row of magnets (see Figures 2.5 and 2.6), since the circular path for electrons has a maximum length in this dip for about 2.75 MeV (see Figure 2.7). (A similar effect would be expected for 6 - 6.5 MeV electrons, but no electrons of this energy are emitted by the beta sources used.) The rise in (measured/calculated) at the beta source end-point energy and the existence of counts beyond the end point are due to bremsstrahlung background and possibly some contribution from the scattered electrons. The measured spectra in Figure 3.6 thus show good agreement with that calculated for the beta sources but show an important background at higher energies.

The addition of the anti-scattering baffles has only a minor effect on the beta spectra but does reduce the higher energy background by a factor of 2-3, as shown in Figure 3.8. The dip in the Ru-Rh-106 spectrum between 2 and 3 MeV is accentuated somewhat because now a baffle, which does eliminate some non-scattered electrons, adds to the magnetic field dip effect at 2.75 MeV. It is expected that a flight unit magnet assembly, which would not have the gap between the magnet rows (see Section 4), would have a more uniform magnetic field and thus not show significant non-uniformities in spectral response. Any non-uniformities that remain will, however, not be important since the

TABLE 3.2

**Electron Transmission after Multiple Scattering In Air**

| Electron Energy (MeV) | $(v/c)^2$ | $(pv)^2$ (MeV) | $\langle\theta^2\rangle$ [a] (radians)$^2$ | $P(r \leq 0.318)$ [b] | $P_1(h)$ [c] $= \sqrt{P(r \leq 0.35)}$ |
|---|---|---|---|---|---|
| 1.5 | 0.9354 | 3.539 | 0.02687 | 0.0239 | 0.970 |
| 2.0 | 0.9586 | 5.794 | 0.01634 | 0.0390 | 0.939 |
| 3.0 | 0.9788 | 11.810 | 0.00799 | 0.0782 | 0.888 |
| 5.0 | 0.9914 | 29.85 | 0.00315 | 0.1867 | 0.770 |

[a] Calculated for $0.0259$ g/cm$^2$ of air ($Z = 7.22$, $A = 14.485$)(Eq. (3.8))

[b] Calculated for $\langle\theta^2\rangle$ and $y = 21.59$ (Eq. 3.10).

[c] Calculated for a path length of $\pi r_e$, with $\langle\theta^2\rangle$ varying with this path length. See text.

---

TABLE 3.3

**Comparison of Measured and Calculated Beta Source Spectra**

| Electron Energy (MeV) | $dJ_e(E)/dE$ in el/(cm$^2$ - sec - sr - MeV)* | | | | | |
|---|---|---|---|---|---|---|
| | Sr-Y-90 | | | Ru-Rh-106 | | |
| | Calculated (Ref. 3.2) | Measured (Fig. 3.6) | $\left(\dfrac{Measured}{Calculated}\right)$ | Calculated (Ref. 3.2) | Measured (Fig. 3.6) | $\left(\dfrac{Measured}{Calculated}\right)$ |
| 1.75 | 3.47 + 6 | 2.41 + 6 | 0.70 | 1.20 + 6 | 1.27 + 6 | 1.06 |
| 2.00 | 1.23 + 6 | 1.51 + 6 | 1.23 | 1.01 + 6 | 1.01 + 6 | 1.00 |
| 2.25 | 0.00 | 4.94 + 5 | ---- | 8.12 + 5 | 6.40 + 5 | 0.79 |
| 2.50 | --- | 1.66 + 5 | ---- | 5.88 + 5 | 4.33 + 5 | 0.74 |
| 2.75 | | | | 3.92 + 5 | 2.36 + 5 | 0.60 |
| 3.00 | | | | 1.99 + 5 | 1.68 + 5 | 0.84 |
| 3.25 | | | | 5.60 + 5 | 1.14 + 5 | 2.04 |
| 3.50 | | | | 0.00 | 7.07 + 4 | ---- |

* $3.47 + 6 \equiv 3.47 \times 10^6$, etc.

flight unit would be calibrated directly with electrons from an accelerator.

The electron energy loss spectra in the 1,000 μm thick PSD are shown in Figure 3.7 and show a peak near 275 keV. For 1.6 to 4.4 MeV, using the stopping powers for Si in Ref. 3.3, electrons should deposit an average energy of 360 keV. From Ref. 3.1, pp. 252 - 267, it is found that for relativistic electrons the most probable energy loss can be written as

$$\Delta E_p = W_1 \left[ \ln \left( \frac{mc^2 \beta^2 W_1}{I^2 (1 + \beta^2)} \right) - \beta^2 - K \right] \tag{3.12}$$

where

$$W_1 = 0.3006 \ \frac{Z\,t}{A} \ \frac{mc^2}{\beta^2} \tag{3.13}$$

with $mc^2$ the electron rest mess in eV, $\beta = v/c$ is the electron velocity divided by the velocity of light, I is the average excitation potential (in eV) of material Z, A, of thickness $t(g/cm^2)$, and $K \approx 0.355$ is a constant. For 1,000 μm of Si (Z = 14, A = 28.086, t = 0.233 g/cm²) and 2 MeV electrons this gives

$$\Delta E_p \ (2 \text{ MeV el}) = 270 \text{ keV} \tag{3.14}$$

which is in close agreement with the measurements. As already mentioned when discussing Figures 3.4 and 3.5 (Section 3.2), the bremsstrahlung background appears to have a higher average energy than the direct electrons, so a 100 - 150 keV threshold, well below the 275 keV peak, gives the best signal/ noise ratio. A threshold below 100 keV will not further improve this ratio. Use of a thinner PSD would, however, require a lower threshold and introduce more noise in the position signal calculation. The measured electron energy loss distributions are also in reasonable agreement with the calculations of Ref. 3.4.

The final configuration uses a 200 μm Si detector in the entrance colli- mator to provide a coincidence signal. The average energy loss for 1.6 to 4.4 MeV electrons is about 71 keV (from data in Ref. 3.3), while the most probable energy loss from (3.12) is 48 keV. Energy loss measurements with a 50 keV threshold show the most probable energy loss to be about 50 keV or less (Figure 3.9) and are thus in agreement with calculations. Actual coin- cidence measurements with the 200 μm and PSD detectors showed that a 15 keV threshold on the 200 μm detector is necessary to give a reasonable detection efficiency. For the straight line arrangement, the maximum coincidence detection efficiency is only about 10% and is due to the multiple scattering of electrons in the 200 μm detector. The multiple scattering in the 200 μm de- tector spreads the electron beam so that only about 10% of those producing large pulses pass through the collimator in front of the PSD.

Use of the 200μm detector in the magnet assembly, with the complete set-up as shown in Figure 3.1, gives the results shown in Figures 3.12 and 3.13. A rough calculation of the multiple scattering effect of the 200 μm de- tector gives a reduction of about a factor of 10. The measured reduction is

about a factor of 4 for no coincidence and an additional factor of 3 with coincidence. The factor of 4 is considered reasonable agreement with the calculated 10, since the complete scattering effect is difficult to calculate because the 200 μm detector scattering adds on to the air scattering. The factor of 3 coincidence reduction is less than the factor of 10 for the straight line geometry. The coincidence reduction results from the correlation between angular scattering and energy loss. Electrons lose energy by scattering, so those electrons which go through the 200 μm detector on the straightest paths, and hence, are most likely to reach the PSD, also are likely to have the lowest energy losses in the 200 μm detector.

The net result of adding the coincidence detector is to reduce the geometric factors by nearly a factor of 10. It also reduces the higher energy background by more than order of magnitude and so improves the signal/noise ratio. The spectra in Figures 3.12 and 3.13 show significantly improved behavior at the beta end-point energies.

A minor problem occurs with the low energy threshold (15 keV) required for the 200 μm detector. This is about the limit of what can be achieved with present room-temperature preamplifiers. Use of a thicker detector would raise this threshold, but it would also increase multiple scattering effects; therefore, no increase in detection efficiency is likely to result. The 200 μm detector is quite probably near the optimum thickness.

Placing the 200 μm detector nearer to the collimator exit aperture ($A_2$ in Figure 3.14) would increase the efficiency somewhat since the magnetic focusing in the $r_c$ plane would nullify one direction of scattering. This would also increase the number of electrons striking the magnet poles and so increase background from bremsstrahlung and scattered electrons. This would thus not be likely to increase the signal/noise ratio for detecting high energy electrons in the presence of low energy electrons.

The final configuration, Figure 3.14, is thus close to the best configuration for the Magnetic Electron Spectrometer. With additional lead shielding for reduction of bremsstrahlung background, and a possible scintillator behind the PSD'S, this is the final design configuration, on which the preliminary flight unit design is based.

## 4. PRELIMINARY DESIGN OF A FLIGHT UNIT MAGNETIC ELECTRON SPECTROMETER

The results in Section 3 allow a preliminary design for a flight unit magnetic electron spectrometer to be made. The properties of this flight unit can be specified with reasonable accuracy. The flight unit magnet arrangement is shown in Figure 4.1. The design uses the same iron yoke design as the test magnet assembly but uses some extra magnets to improve the measurement at 10 MeV. The design uses 19 - 1 1/16 x 1 1/16 x 1/2 inch, 3 - 11/16 x 1/2 x 1/2, and 2 - 1/2 x 1/2 x 1/2 inch magnets on each plate. The magnets are

35
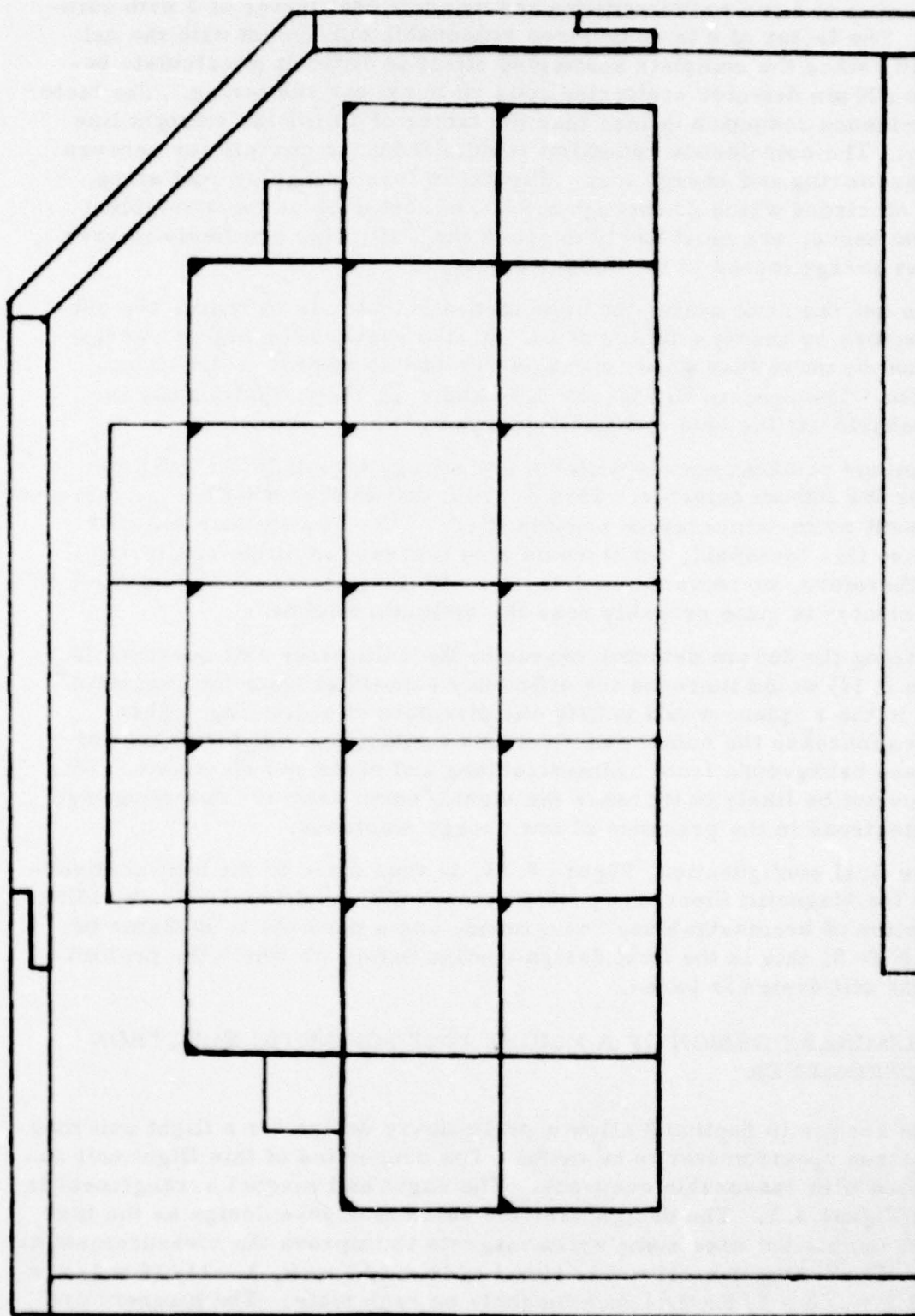
Figure 4.1 Magnet Arrangement for Flight Unit Magnet Assembly.

selected from a larger number on the basis of magnet field measurements to produce a more uniform field. The largest magnets have a tab ground off on one corner to allow the use of holding screws during and after assembly. Elimination of the screw gaps (Figure 2.2) should, in combination with magnet selection, allow the magnet assembly to have an average field in the gap of 4.50 $\pm$ 0.15 kg, a $\pm$3% uniformity.

The paths of 1 to 10 MeV electrons in the magnet gap are shown in Figure 4.2. There is sufficient edge field to allow magnetic focusing even for the 10 MeV electrons. With the field uniform to $\pm$3%, deviations from the paths in Figure 4.2 should not be significant at the performance level. The effects of fringing fields will cause slight changes in the curved and straight paths at the magnet pole edges but should have only a small effect on the exit positions for 1 to 10 MeV electrons.

The complete entrance collimator, detector, and baffle design is shown in Figure 4.3. The entrance collimator contains a front magnet assembly to shield the coincidence detector from electrons below 100 - 200 keV and so avoid pile-up problems from large fluxes of low energy electrons. The entrance collimator is made from aluminum to reduce bremsstrahlung production. The 200 $\mu$m surface barrier detector has a thin aluminum foil light shield, which adds negligibly to the electron scattering of the detector itself.

The detector at the magnet exit line is designed to be a strip surface barrier detector, 1,000 $\mu$m thick, and segmented into 12 individual rectangular detectors. The detector strip need not be a single piece of silicon but must be mounted with only a small dead section between adjacent strips. The detector array is shielded from behind, top, bottom, and from the entrance collimator by lead to reduce the bremsstrahlung background. A shielded detector at the high energy end provides a background measurement.

The strip detector is designed with 7 segments of 1 cm width at the low energy end, 4 segments of 2 cm width at the high energy end, and a 1 cm wide segment for background measurement. The junctions between adjacent segments have a 0.25 inch long strip of 1/16 inch copper extending to the magnet pole edges as an electron shield. Five baffles of 30 degree arc length are installed as shown in Figure 4.3. The baffles are limited to 30° to reduce their interference with the magnet focusing properties.

The segmented strip detector design was chosen over the use of position sensitive detectors for a number of reasons. The use of position sensitive detectors would have required at least three (3), which requires six (6) preamplifier/amplifier chains, already half of the requirement for the segmented strip. The position calculation electronics are easily the equivalent of the remaining six (6) preamplifier/amplifier chains; therefore, the segmented strip does not require a significant amount of additional electronic components.

The segmented strip detectors can be made to operate with a total response time of less than one microsecond, while the position calculation electronics typically requires several microseconds. Thus, the segmented strip can handle count rates (and fluxes) nearly an order of magnitude higher than

37
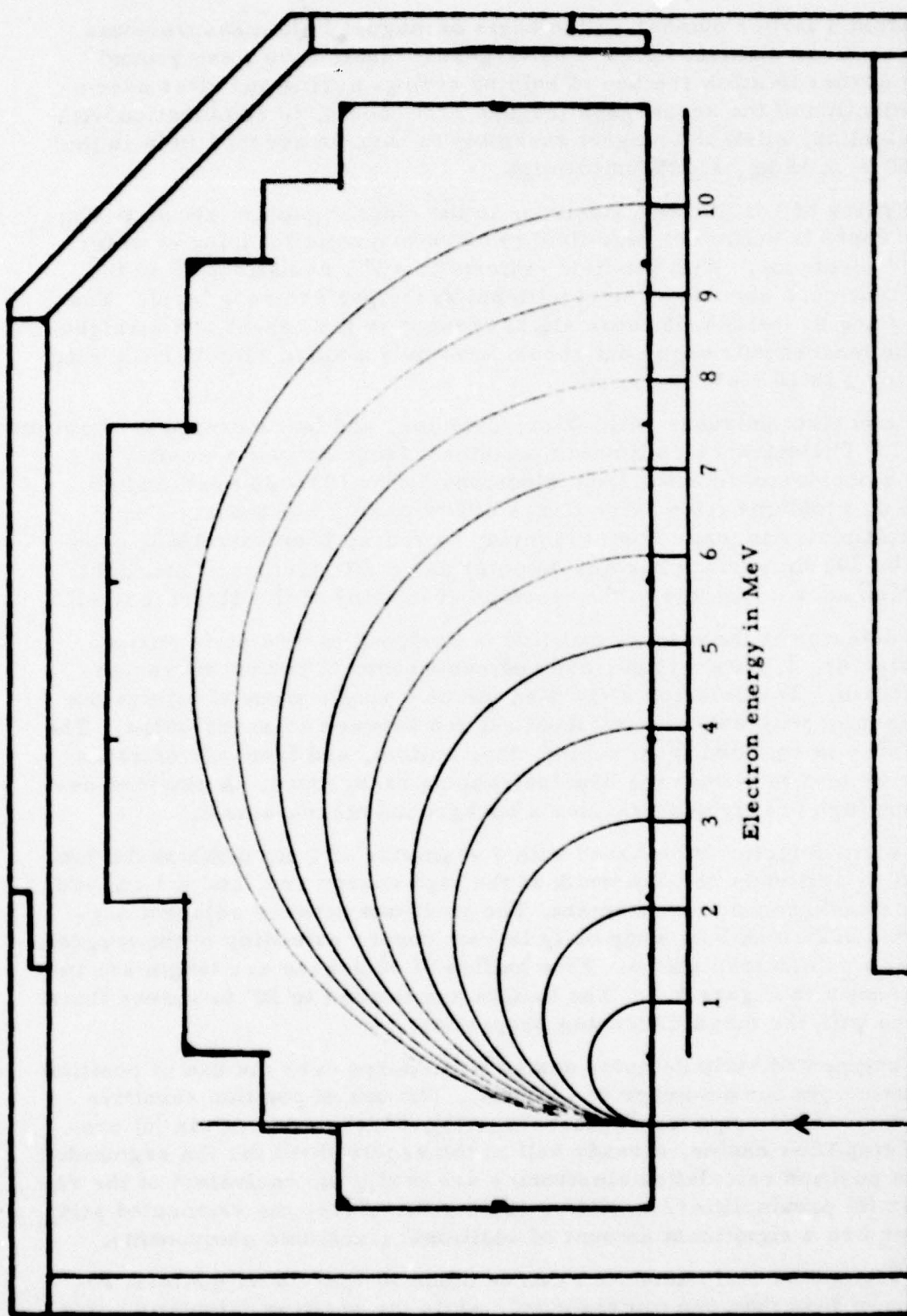
Figure 4.2  Paths of 1 to 10 MeV Electrons in Flight Unit Magnet Assembly

Electron energy in MeV
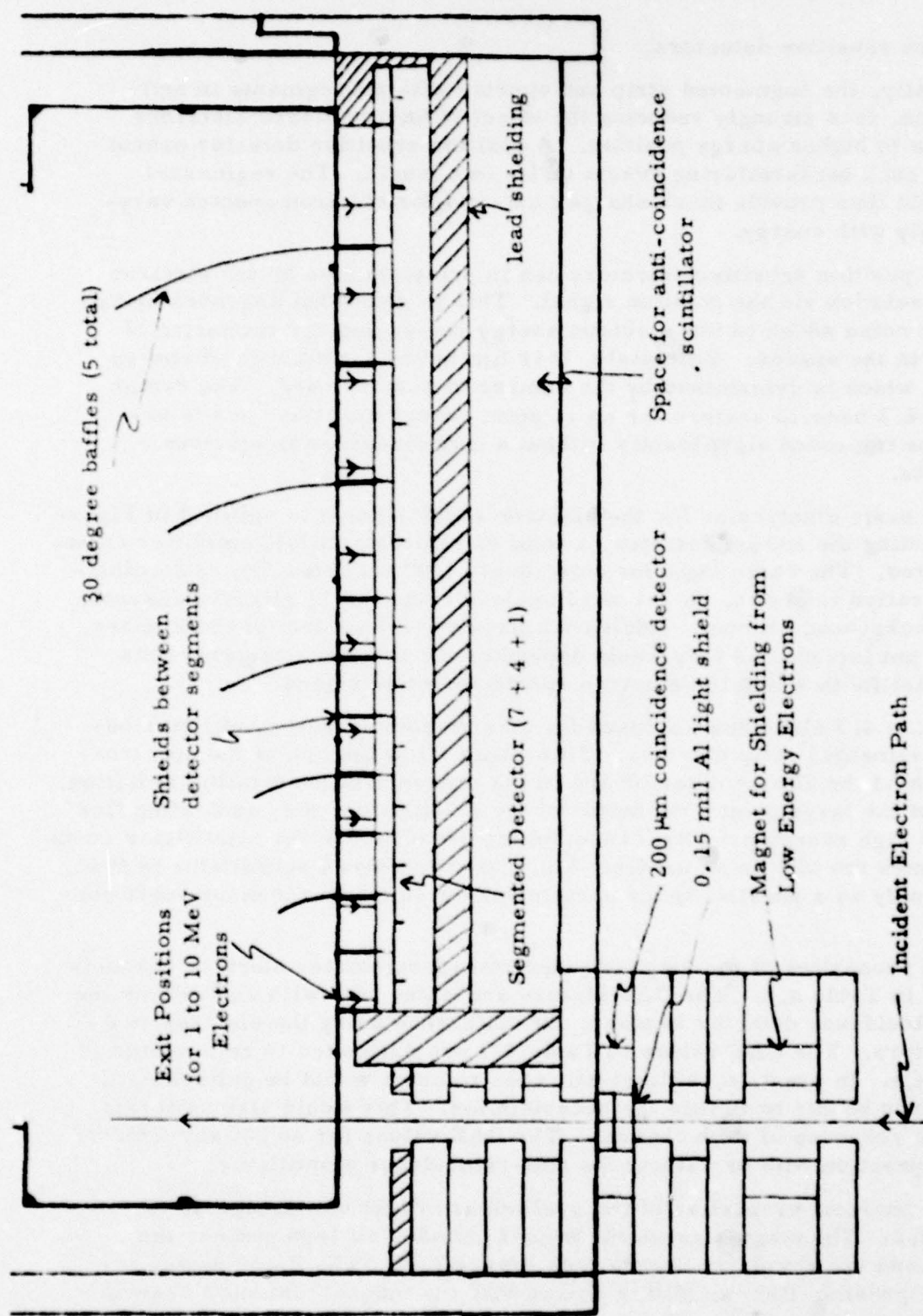
Figure 4.3  Preliminary Design for Entrance Collimator, Detectors, and Baffles

30 degree baffles (5 total)

Shields between
detector segments

Exit Positions
for 1 to 10 MeV
Electrons

lead shielding

Space for anti-coincidence
scintillator

Segmented Detector (7 + 4 + 1)

200 μm coincidence detector

0.15 mil Al light shield

Magnet for Shielding from
Low Energy Electrons

Incident Electron Path

the position sensitive detectors.

Finally, the segmented strip can operate with all segments in anti-coincidence, thus strongly reducing the effect of backscattered electrons from a low to higher energy position. A position sensitive detector cannot eliminate such backscattering events on its own length. The segmented strip should thus provide much sharper cut-offs for electron spectra varying strongly with energy.

The position sensitive detectors can in principle give better electron energy resolution via the position signal. This is somewhat degraded by the electronic noise added to low electron energy losses and the scattering of electrons in the silicon. Ultimately, it is limited by the number of energy channels, which is determined by the number of scalers used. The design in Figure 4.3 uses 12 scalers for an 11 point energy spectrum and is unlikely to be improved significantly without a large increase in electronic components.

The basic electronics for the electron spectrometer is outlined in Figure 4.4. Counting the 200 μm detector, a total of 13 preamplifier/amplifier chains are required. The basic logic for coincidence (200 μm detector)/anti-coincidence operation is shown. A set of 12 scalers count the 11 electron channels and one background channel. Additional circuitry for control of cycle times, etc., are not included as they would depend on the interface requirements for the satellite in which the electron spectrometer is placed.

Figure 4.3 also shows a space for an anti-coincidence scintillator behind the segmented strip detector. This would allow the use of the spectrometer without the 200 μm detector and in the presence of penetrating radiation. Because of the large geometric factor of the scintillator, the penetrating flux (generally high energy protons) cannot be too great before the scintillator count rate becomes too high to be usable. The anti-coincidence scintillator is thus indicated only as a possibility for certain very specific flux measurement conditions.

The properties of the magnetic electron spectrometer electron channels are listed in Table 4.1. The GΔE factors are listed both with and without the 200 μm coincidence detector in place, the difference being the electron scattering factors. The GΔE values in Table 4.1 are estimated to be accurate to a factor of 3. In practice, a flight unit spectrometer would be calibrated with electron beams to reduce the uncertainties. This would also calibrate the energy response of each channel. The GΔE values for no 200 μm detector hold for operation with or without the anti-coincidence scintillator.

The physical properties of the preliminary flight unit design are given in Table 4.2. The magnet assembly weight includes all iron pieces, the magnets, and the aluminum braces (see Figure 2.3). The listed design includes the preamplifier/amplifier chains with the magnet/detector assembly and a separate electronics unit for power/signal processing. If the electronics
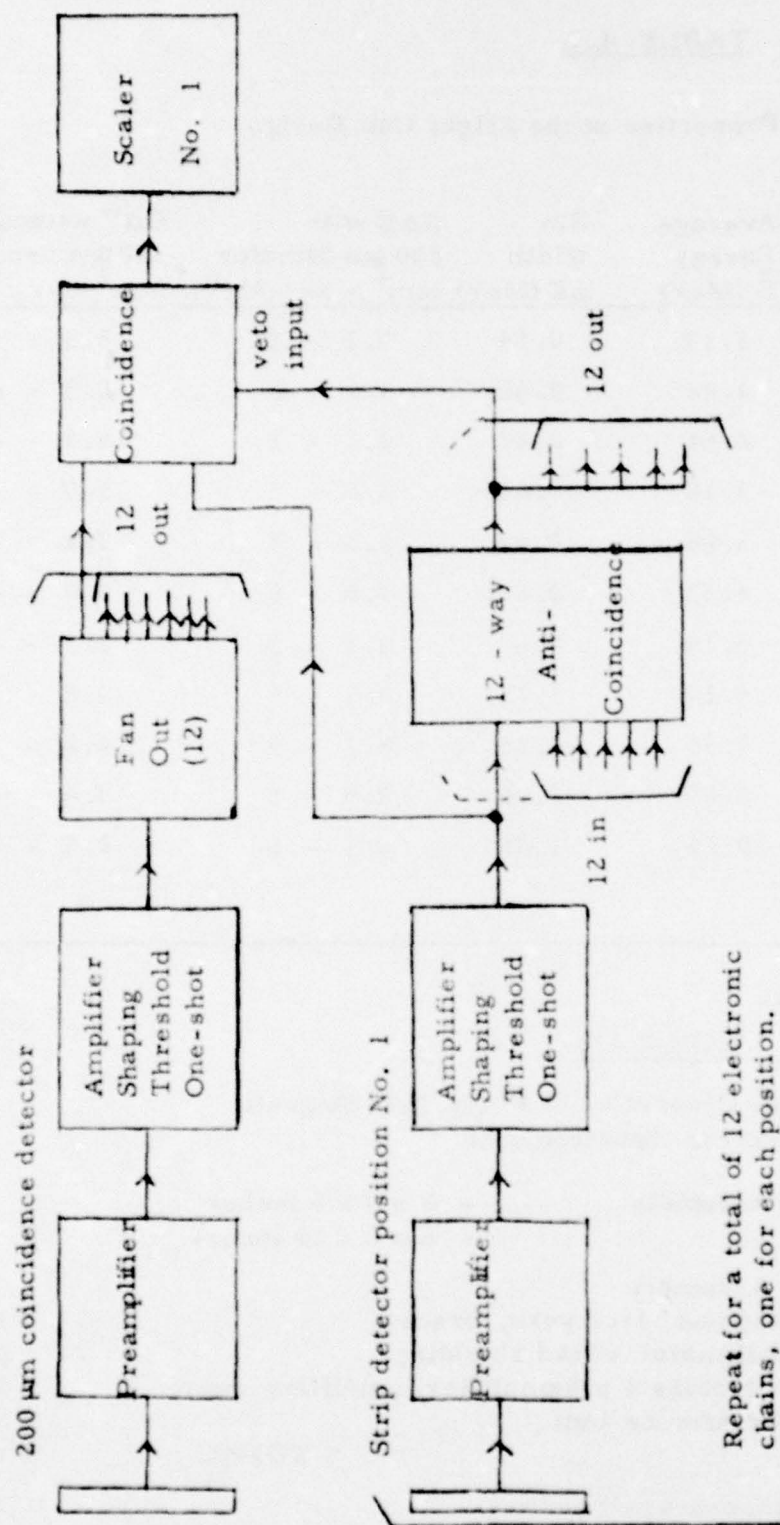
Figure 4.4  Basic Electronic Block Diagram for the Electron Spectrometer

41

## TABLE 4.1

Electron Detection Properties of the Flight Unit Design

| Electron Bin Number | Electron Energy Range (MeV) | Average Energy $\overline{E}$ (MeV) | Bin Width $\Delta E$ (MeV) | $G\Delta E$ with 200 $\mu$m detector ($cm^2$ - sr - MeV)[*] | $G\Delta E$ without 200 $\mu$m detector ($cm^2$ - sr - MeV)[*] |
|---|---|---|---|---|---|
| 1 | 0.87 - 1.51 | 1.19 | 0.64 | 7.1 - 6 | 5.5 - 4 |
| 2 | 1.51 - 2.17 | 1.84 | 0.66 | 1.5 - 5 | 5.3 - 4 |
| 3 | 2.17 - 2.84 | 2.51 | 0.67 | 2.2 - 5 | 4.5 - 4 |
| 4 | 2.84 - 3.51 | 3.18 | 0.67 | 2.8 - 5 | 3.9 - 4 |
| 5 | 3.51 - 4.18 | 3.85 | 0.67 | 3.3 - 5 | 3.4 - 4 |
| 6 | 4.18 - 4.85 | 4.52 | 0.67 | 3.8 - 5 | 3.0 - 4 |
| 7 | 4.85 - 5.52 | 5.19 | 0.67 | 4.1 - 5 | 2.7 - 4 |
| 8 | 5.52 - 6.87 | 6.20 | 1.35 | 8.5 - 5 | 4.8 - 4 |
| 9 | 6.87 - 8.22 | 7.55 | 1.35 | 8.7 - 5 | 4.2 - 4 |
| 10 | 8.22 - 9.57 | 8.90 | 1.35 | 8.9 - 5 | 3.5 - 4 |
| 11 | 9.57 - 10.92 | 10.25 | 1.35 | 9.1 - 5 | 2.9 - 4 |
| 12 | Background | | | | |

[*] $7.1 - 6 = 7.1 \times 10^{-6}$, etc.

## TABLE 4.2

Estimated Physical Properties of Flight Unit Magnetic Electron Spectrometer

Size:  Magnet/Detector Assembly  - 8 x 9 x 5 inches
       Electronics Unit  - 6 x 6 x 10 inches

Weight:  Magnet/Detector Assembly
         Magnets, iron yoke, braces - 19 lbs.
         Collimator + lead shielding - 3 lbs.
         Detectors + preamplifier/amplifier chains - 2 lbs.
         Electronics Unit - 6 lbs.
         TOTAL =  30 lbs.

Power Consumption - from spacecraft buss  - 10 W

Note: If the electronics unit is combined with the magnet/detector assembly, the combined size would be about 8 x 9 x 10 inches, and a small weight saving would result. The actual design of 2 or 1 housings can be done to fit spacecraft requirements.

42

unit can be combined with the magnet/detector assembly, a small savings in weight could be achieved. This latter design would be preferable from an electronics design viewpoint as it eliminates external signal cables for the detectors. The actual use of 2 or 1 housings can be done according to spacecraft requirements. The power consumption of 10W is input power to the DC/DC converter from the spacecraft buss and covers all instrument requirements.

## 5. CONCLUSIONS

A preliminary design of a flight unit magnetic electron spectrometer for less than 1 to greater than 10 MeV electrons has been described. The design is based on an extensive series of tests with a rare-earth cobalt magnet assembly and position sensitive solid state detectors. These tests proved that a magnet assembly could be built to analyze to at least 10 MeV electrons. The major background sources were found to be internally scattered electrons, and bremsstrahlung, both internally and externally generated. For flight into the inner belt, background due to penetrating protons would also have to be considered.

The final configuration uses a lead-shielded segmented-strip surface barrier detector at the magnet exit plane and a 200 μm transmission detector in the entrance collimator for coincidence measurement. Scattered electron detection is reduced by baffles in the magnet assembly. The segmented-strip detector arrangement was selected because it is no more complex than the position sensitive detector arrangement but allows higher count rates and provides anti-coincidence discrimination against low energy electrons which are backscattered to a higher energy position.

The final design uses either two or one housings with a total volume of about $8 \times 9 \times 10 = 720$ inches$^3$, a total weight of about 30 lbs., and a total power consumption of 10 W.

# REFERENCES

1.1 Mozer, F. S., D. D. Elliott, J. D. Mihalov, G. A. Paulikas, A. L. Vampola, and S. C. Freden, "Preliminary Analysis of the Fluxes and Spectrums of Trapped Particles after the Nuclear Test of July 9, 1962," J. Geophys. Res. 68, 641-9(1963).

1.2 Mihalov, J. D, F. S. Mozer, and R. S. White, "Artificially Injected Electrons at Low Altitudes," J. Geophys. Res. 69, 4003-13(1964).

1.3 Paolini, F. R., G. C. Theodoridis, and W. F. Welsh, "Satellite Instrumentation for Charged Particle Measurements IIL Scintillation Spectrometer for Relativistic Electrons," IEEE Trans. Nuc. Sci. NS-15, #1, 200-4(1968).

1.4 Paolini, F. R., G. C. Theodoridis, and W. F. Welsh, "Satellite Instrumentation for Charged Particle Measurements IL Magnetic Analyzer for 0.1 to 1.0 MeV Electrons," IEEE Trans. Nucl. Sci. NS-15, #1, 194-9(1968).

1.5 Vampola, A. L., "Energetic Electrons at Latitudes above the Outer-Zone Cutoff," J. Geophys. Res. 74, 1254-69(1969).

1.6 West, H. I., Jr., R. M. Buck, and J. R. Walton, "Electron Pitch Angle Distributions throughout the Magnetosphere as Observed on Ogo 5", J. Geophys. Res. 78, 1064-81(1973).

3.1 Segre, E., Editor, "Experimental Nuclear Physics," Vol. I, Wiley, New York (1953):

3.2 Hogan, O. H., P. E. Zigman, and J. L. Mackin, "Beta Spectra, II. Spectra of Individual Negatron Emitters," USNRDL-TR-802 (16 December 1964).

3.3 Berger, M. J., and S. M. Seltzer, "Additional Stopping Power and Range Tables for Protons, Mesons, and Electrons," NASA SP-3036 (1966).

3.4 Berger, M. J., S. M. Seltzer, S. E. Chappell, J. C. Humphreys, and J. W. Motz, "Response of silicon detectors to monoenergetic electrons with energies between 0.15 and 5.0 MeV," Nucl. Instr. and Meth. 69, 181-193(1969).

A.1 Coggeshall, N. D., J. Appl. Phys. 18, 855 (1947).

A.2 Coggeshall, N. D., and M. Muskat, Phys. Rev. 66, 187 (1944).

## Appendix A

## The Trajectory of a Charged Particle in the
## Fringing Field of a Magnet for Arbitrary Incidence Angle

### A.1 Introduction

It is often necessary to find the trajectory of a particle in a magnet's fringing field, similar to that shown in Fig. A.1. Here

$$h(y) = \frac{H(y)}{H_o} \tag{A.1}$$

where $H(y)$ is field intensity at a distance $y$ (perpendicular to the pole face) from a point inside the pole boundary at which $H(y)$ may be assumed to have its uniform-field value $H_o$. With reference to Fig. A.2, the general problem is that of finding, for known $h(y)$, the trajectory $x(y)$ and the angle $\epsilon(y)$ made by a tangent to the trajectory with the uniform field boundary.

The only value of $\epsilon(y)$ that is normally of significance is $\epsilon_o \equiv \epsilon(y=0)$. However, $x(y)$ is often of interest for arbitrary $y$, in order to determine whether the trajectory intercepts collimators etc. located at specific values of $y$.

The approach taken here for arbitrary incidence angle $\epsilon_i$ is similar to that of Coggeshell (Ref. A.1) and Coggeshall and Muskat (Ref. A.2) for normal incidence ($\epsilon_i=0$). It is assumed that H is a function $H(y)$; it does not depend on x. Clearly, this simplifies the problem considerably. In a realistic case, it is a good approximation if the distance $x_\infty$ at which the integration must be started is small compared to the x-dimension of the magnet pole faces. Of course, in order to place the results in an external reference frame it is necessary to specify $y_p$, the uniform field-pole boundary distance. As seen in Fig. A.1, for that particular magnet (pole faces small compared to gap width; yoke sufficient to contain external field quite well) this distance was about 1.6 gap widths. Hence, in addition to $h(y)$, it will be assumed that $y_p$ is also specified. The field reversal shown in Fig. A.1 is caused by the fact that the entrance aperture of the assembly penetrates the yoke.
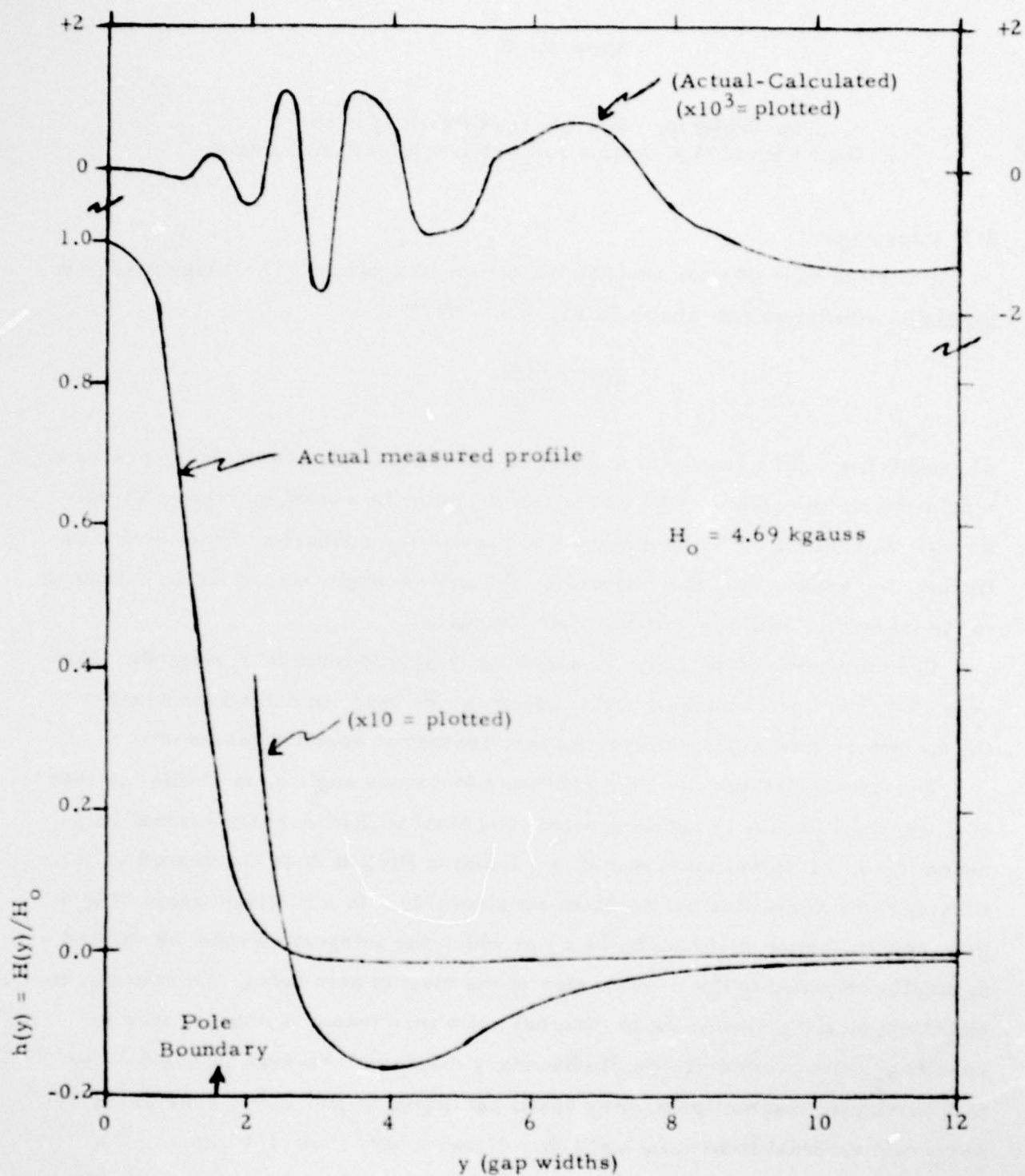
Fig.A.1 h(y) vs y, with Results of Fit, for
Actual Magnet.

Fig.A.2 Geometry for Calculation of Trajectory x(y) in Fringing Field H(y).

47

The integration is started at the point $x_\infty(y_\infty)$, where the particle trajectory makes the initial angle $\epsilon_i$ with the y-axis. From simple geometrical considerations, $x_i(y)$ can be found. Then $\Delta x(y)$, the fringing field induced deviation, can be added to obtain $x(y)$

$$x(y) = x_i(y) + \Delta x(y) \tag{A.2}$$

$$= x_{io} + y\tan\epsilon_i + \Delta x(y) \tag{A.3}$$

where

$$x_{io} = x_\infty - y_\infty \tan\epsilon_i, \tag{A.4}$$

in terms of the chosen initial conditions $x_\infty$, $y_\infty$, and $\epsilon_i$. Thus, in terms of these conditions and the deviation $\Delta x(y)$, the trajectory $x(y)$ can be found from (A.3).

Conceptually, it is convenient to consider the problem as above. However, in the procedure below $x(y)$ is determined directly, as is $\epsilon(y)$. A particular analytical function for $h(y)$ is then shown to fit the curve in Fig.A.1. This function is used in the general equation for $\epsilon(y)$, allowing an entirely analytical result for that quantity. It is found that this then yields a result requiring only one simple numerical integral for $x(y)$.

A.2  General Equations for $x(y)$ and $\epsilon(y)$.

The differential equations for a charged particle of initial velocity $v_o$ and radius of curvature $r_o$ in the median plane uniform field (inside magnet) are

$$\ddot{x} = \frac{-v_o}{r_o} h(y)\dot{y} \tag{A.5}$$

$$\ddot{y} = \frac{v_o}{r_o} h(y)\dot{x} \tag{A.6}$$

Multiplying the first by $\dot{x}$, the second by $\dot{y}$, yields

$$-\dot{x}\ddot{x} = \dot{y}\ddot{y}$$

or

$$-\frac{d\dot{x}^2}{dt} = \frac{d\dot{y}^2}{dt}$$

48

Thus

$$\dot{x}^2 + \dot{y}^2 = v_o^2 \tag{A.7}$$

and (choosing the proper sign for $\dot{y}$)

$$\dot{y} = -\left(v_o^2 - \dot{x}^2\right)^{\frac{1}{2}} \tag{A.8}$$

Given $\dot{x}$, $\dot{y}$ is then found from (A.8). From (A.5)

$$\dot{x}(y) = -\frac{v_o}{r_o} \int_{y_\infty}^{y} h(y')dy' + \dot{x}_\infty \tag{A.9}$$

Thus, if we define the quantity

$$R(y) = -\int_{y_\infty}^{y} h(y')dy' = \int_{y}^{y_\infty} h(y')dy' \tag{A.10}$$

Then

$$\dot{x} = \frac{v_o}{r_o} R(y) - v_o \sin \epsilon_i \tag{A.11}$$

Division of (A.11) by (A.8) yields

$$\frac{\dot{x}}{\dot{y}} = \frac{dx}{dy} = \tan\epsilon(y) = \frac{r_o \sin \epsilon_i - R(y)}{\left[r_o^2 - \left(r_o \sin \epsilon_i - R(y)\right)^2\right]^{\frac{1}{2}}} \tag{A.12}$$

This equation thus defines $\epsilon(y)$, as sought. If the analytic expression chosen to fit $h(y)$ is integrable in (A.10), $\epsilon(y)$ is defined analytically from (A.12). Although $\tan\epsilon(y)$ is required to find $x(y)$ below, the angle $\epsilon_o$ at entry to the uniform field is more easily determined - as can be seen from (A.12) - from

$$\sin \epsilon_o = \sin \epsilon_i - R(0)/r_o \tag{A.13}$$

$x(y)$ can now be found by integration of (A.12), which must be carried out numerically for any reasonably accurate $h(y)$ representation. The result is

49

$$\int_{x_\infty}^{x} dx' = x - x_\infty = \int_{y_\infty}^{y} \tan\epsilon(y')dy' \qquad (A.14)$$

Thus,

$$x(y) = x_\infty + \int_{y_\infty}^{y} \tan\epsilon(y')dy' \qquad (A.15)$$

with $\tan\epsilon(y)$ given by (A.12). Thus, at entry to the uniform field

$$x_o \equiv x(0) = x_\infty + \int_{y_\infty}^{0} \tan\epsilon(y')dy' \qquad (A.16)$$

In summary, for any $h(y)$, $R(y)$ is defined by (A.10). $\epsilon_o$ and $x_o$ are found from (A.13) and (A.16), and the trajectory $x(y)$ from (A.15) with $\tan\epsilon(y)$ obtained from (A.12).

A.3 Results for $R(y)$ with an Analytical Approximation for $h(y)$.

Let it be assumed that $h(y)$ can be written

$$h(y) = e^{-Ky} \sum_{j=1}^{N_i} a_j y^{j-1} \qquad (A.17)$$

That this is a good approximation for the dependence of h on y in Fig. 1 is shown in Section A.5 below. The number of terms $N_i$ that must be used is $\leq 9$. In order for $h(y)$ to have the value unity at $y=0$, we must have $a_1 = 1$. A further condition is obtained by requiring that $dh/dy=0$ at $y=0$, which requires $K=a_2$. These conditions are used in Section A.4 in development of a least square procedure for determining the constants $a_j$ that "best fit" an experimental $h(y)$ curve such as Fig.A.1.

Here, (A.17) is substituted into (A.10) and integrated. After some re-arrangement the result can be written as follows, assuming $y_\infty \to \infty$.

$$R(y) = \frac{e^{-Ky}}{K} \sum_{j=1}^{N_i} g_j y^{j-1} \tag{A.18}$$

where

$$g_j = \frac{1}{(j-1)!} \sum_{s=j}^{N_i} a_s \frac{(s-1)!}{K^{s-j}} \tag{A.19}$$

Thus, given all of the $a_j$ and K, the $g_j$ can be determined from (A.19). Insofar as the trajectory determination is concerned, further reference to the $a_j$ need not subsequently be made, since only the value of R(y) from (A.18) is needed in (A.12) for use in (A.15). Note that

$$R(0) = g_1/K \tag{A.20}$$

so that the entrance angle $\epsilon_o$ is easily found from (A.13) once the h(y) fit (A.17) has been completed.

A.4 Least Square Procedure for Fitting h(y).

Because h(y) contains a non-linear parameter K, the usual least square procedure must be modified somewhat. It is not difficult to find the general range of values that K must have, given the experimental data $h_i$, $y_i$; $i=1$, $N_p$; that must be fitted. Here we shall have, as noted above,

$$\left. \begin{array}{l} a_1 = 1 \\ K = a_2 \end{array} \right\} \tag{A.21}$$

There are, therefore, $N_i - 1$ coefficients to be determined from the $N_p$ values of $h(N_p > N_i)$.

In the case of interest here, then,

$$h(y) = e^{-a_2 y} \sum_{j=1}^{N_i} a_j y^{j-1}; \; a_1 = 1 \tag{A.22}$$

Because the deflection depends on the <u>magnitude</u> of $h(y)$, the trajectory that deviates least from that which would actually occur in the field $h(y)$ should be obtained by minimizing the actual differences in field <u>magnitudes</u>, rather than minimizing the <u>fractional</u> differences. Thus, we write the sum of the squared deviations as

$$\Delta^2 = \sum_{i=1}^{N_p} \left| h(y_i) - h_i \right|^2 \tag{A.23}$$

The procedure used here is to vary $a_2$ throughout a selected range of values. For each given $a_2$ the values of $a_j$ ($j=3$, $N_i$) are determined that provide the best least square fit to (A.23), and the associated value $\Delta(a_2)^2$ is found. The optimum value of $a_2$, and associated $a_j$ ($j = 3$, $N_i$), is that for which $\Delta(a_2)^2$ is minimum.

For convenience we let $c_{j-1} = a_j$, $j \rightarrow j-1$, and $J_m = N_i - 1$, and obtain

$$\Delta^2(c_1) = \sum_{i=1}^{N_p} \left[ e^{-c_1 y_i} \sum_{j=2}^{J_m} c_j y_i^{\,j} - b_i(c_1) \right]^2 \tag{A.24}$$

where

$$b_i(c_1) = h_i - (1 + c_1 y_i) e^{-c_1 y_i} \tag{A.25}$$

Here we will vary $c_1 (\equiv a_2)$, which defines $b_i(c_1)$ for each $y_i$, and find the $c_j$ ($j = 2$, $J_m$) that minimize $\Delta^2(c_1)$. Proceeding in the usual way by setting

$$\frac{d\Delta^2}{dc_m} = 0; \quad m = 2, J_m \tag{A.26}$$

yields $J_m - 1$ equations of the form below,

$$\sum_{j=2}^{J_m} B_{mj} c_j = B_{m, J_m + 1}; \quad m = 2, J_m \quad \text{(A.27)}$$

where

$$B_{mj} = \sum_{i=1}^{N_p} y_i^{m+j} e^{-2c_1 y_i} \quad \text{(A.28)}$$

$$B_{m, J_m + 1} = \sum_{i=1}^{N_p} y_i^m \left[ h_i - (1 + c_i y_i) e^{-c_1 y_i} \right] e^{-c_1 y_i} \quad \text{(A.29)}$$

The programs used to solve this set of equations with the procedure described are given in Section A.5 below.

A.5  Program Description and Application

In this section the FORTRAN II programs used to fit the h(y) data and to tabulate the results are given, along with results of application to a "typical" h(y) - Fig.A.1. There are two programs:  MAGLSQ. FT and MAGTAB. FT. The first reads in the h(y) data and obtains the least square fit.  The second gives the constants $a_j$ and $g_j$, and tabulates the calculated results for h(y) and R(y).

MAGLSQ. FT is listed in Fig.A.3, with input and output in Tables A.1a and A.1b.

| Statements | Description |
|---|---|
| 0-5 | Read in tabular array of y(j), h(j) for NPT points (Table A.1a).  This program is returned to by MAGTAB, hence it is necessary to decide initially (K) whether to input data on start new iteration. |
| 10-15 | Choose number of max pt to be fitted $N_p$ (fit always starts at j=1) and total number $N_i$ of $a_j$ coefficients (top Table A.1b).  Set up an array P(j, k) needed later. |

53

```
C           MAGLSQ.FT: FIT TO H(Y) FOR MAG ANALYZER,1/9/78.
C           MAX VAL NI IS 9; VAL'S CD<.00001 NEGLECTED(SEE 21 ETC BELOW).
            COMMON NPT,Y,H,NP,NI,JM,C,P,B
            DIMENSION C(9),H(30),Y(30),P(30,16),B(8,9)
            WRITE(1,113)
  1         READ(1,114)K
            IF(K)3,10,15
  3         READ(1,100)NPT
            WRITE(1,111)
            DO 5 J=1,NPT
            WRITE(1,101)J,
  5         READ(1,102)Y(J),H(J)
  10        READ(1,110)NP
            READ(1,112)NI
            JM=NI-1
            M=2*JM
            DO 15 J=1,NPT
            DO 12 K=1,M
  12        P(J,K)=Y(J)**K
  15        CONTINUE
  16        WRITE(1,105)
            READ(1,106)L
            IF(L)1,17,20
  17        READ(1,107)C0,CD,CF
            WRITE(1,108)
            N=0
  19        C1=C0+FLOAT(N)*CD
            GO TO 21
  20        READ(1,103)C1
  21        Z=100.*(C1+.000009)
            I=Z
            Z=Z-FLOAT(I)
            M=1000.*Z
            C1=(FLOAT(I)+FLOAT(M)/1000.)/100.
            C(1)=C1
            D=2.*C1
C           C(J)=A(J+1) IN WRITE-UP. NOW FIND CONSTS.
            DO 30 M=2,JM
            BM=0.
            DO 23 I=1,NP
            Z=C1*Y(I)
            E=0
            IF(Z-86.)22,22,23
  22        E=EXP(-Z)
  23        BM=BM+(H(I)-(1.+Z)*E)*E*P(1,M)
            B(M,JM+1)=BM
            DO 27 J=2,JM
            BM=0.
            DO 25 I=1,NP
            Z=D*Y(1)
            E=0
            IF(Z-86.)24,24,25
  24        E=EXP(-Z)
  25        BM=BM+E*P(I,M+J)
  27        B(M,J)=BM
  30        CONTINUE
C           ALL CONSTS FOUND, SOLVE EQ ARRAY.
```

Fig.A.3  MAGLSQ.FT Listing
(cont. next page)

54

```
           DO 70 K=2,JM
           E=B(K,K)
           I=K
           DO 62 M=K,JM
           IF(B(M,J)-E)62,62,61
61         I=M
           E=B(M,J)
62         CONTINUE
           DO 64 J=K,NI
           E=B(K,J)
           B(K,J)=B(I,J)
64         B(I,J)=E
           DO 66 M=2,JM
66         C(M)=B(M,K)
           DO 69 J=K,NI
           B(K,J)=B(K,J)/C(K)
           DO 68 M=2,JM
           IF(M-K)67,68,67
67         B(M,J)=B(M,J)-C(M)*B(K,J)
68         CONTINUE
69         CONTINUE
70         CONTINUE
           DO 71 J=2,JM
71         C(J)=B(J,JM+1)
C          SOLN COMPLETE FOR C(J),J=2,JM, WITH C1=A2 AS INPUT, AND A1=1.
C          CALC VALUE OF MEAN SQ. DEV.
           D=0.
           DO 75 I=1,NP
           Z=C1*Y(I)
           E=0
           IF(Z-86.)72,72,73
72         E=EXP(-Z)
73         BM=0.
           DO 74 J=2,JM
74         BM=BM+C(J)*P(I,J)
           BM=E*BM-H(I)+(1.+Z)*E
75         D=D+BM**2
           E=SQRT(D/FLOAT(NP))
           IF(L)16,82,80
80         WRITE(1,104)E
           GO TO 84
82         WRITE(1,109)C1,E,D
           N=N+1
           IF(C1-CF)19,16,16
84         CALL CHAIN('MAGTAB')
100        FORMAT('NO. PTS TO TAB.,NPT='I3)
101        FORMAT(I3)
102        FORMAT(2X,F5.2,2X,F6.4)
103        FORMAT('A2='F10.6)
104        FORMAT('M.SQ.DEV.='F10.7)
105        FORMAT(///'SET L=-1;0;1 TO START NEW FIT; ITERATE A2;'
      1    ' CHOOSE A2 AND TABULATE.'/)
106        FORMAT('L='I3)
107        FORMAT('A2 MIN='F10.6,//'DEL A2='F10.6,//'A2 MAX='F10.6)
108        FORMAT(///'MEAN SQUARE DEV. IS FOR NP PTS'//'    A2      M.SQ.DEV.'
      1    '    SUM SQ. DEV.'/)
109        FORMAT(F7.4,2X,F10.7,2X,F12.9)
110        FORMAT('MAX PT TO FIT, NP='I3)
111        FORMAT(///'  J      Y(J)      H(J)'//'III    XX.XX    X.XXXX')
112        FORMAT('TOT. NO. A(J) COEFFICIENTS, NI='I3)
113        FORMAT(///'SET K=-1;0;1 TO INPUT FIT DATA; NP,NI VALUES;'/
      1    ' OR TO START ITERATION.')
114        FORMAT('K='I3)                    55
           END
```

Fig.A.3 (cont.) MAGLSQ. FT Listing

```
. R MAGLSQ


SET K=-1;0;1 TO INFUT FIT DATA; NP,NI VALUES;
OR TO START ITERATION.
K=-1
NO. PTS TO TAB.,NPT=30


   J    Y(J)     H(J)
 I II   XX.XX    X.XXXX
   1    0.50     .9600
   2    1.00     .7100
   3    1.50     .2650
   4    2.00     .0600
   5    2.50     .0055
   6    3.00    -.0130
   7    3.50    -.0155
   8    4.00    -.0160
   9    4.50    -.0155
  10    5.00    -.0130
  11    5.50    -.0100
  12    6.00    -.0080
  13    6.50    -.0060
  14    7.00    -.0045
  15    7.50    -.0035
  16    8.00    -.0030
  17    8.50    -.0025
  18    9.00    -.0020
  19    9.50    -.0018
  20   10.00    -.0017
  21   10.50    -.0016
  22   11.00    -.0015
  23   11.50    -.0014
  24   12.00    -.0013
  25   12.50    -.0012
  26   13.00    -.0011
  27   13.50    -.0010
  28   14.00    -.0009
  29   14.50    -.0008
  30   15.00    -.0007
```

Table A.la. h(y) Input Data for MAGLSQ. FT

```
MAX PT TO FIT, NP=30
TOT. NO. A(J) COEFFICIENTS, NI=9
```

```
SET L=-1;0;1 TO START NEW FIT; ITERATE A2; CHOOSE A2 AND TABULATE.
```

```
L=0
A2 MIN=2.1500
DEL A2=0.0200
A2 MAX=2.1900
```

Note: A separate broad range scan on $a_2$ (not shown) between 1.0 and 4.0 found the region 2.15 to 2.19 to contain the minimum. Shown here is the scan of that region.

```
MEAN SQUARE DEV. IS FOR NP PTS
   A2      M.SQ.DEV.   SUM SQ. DEV.
 2.1500   0.0009633   0.000027836
 2.1700   0.0009463   0.000026866
 2.1900   0.0011362   0.000038726
```

```
SET L=-1;0;1 TO START NEW FIT; ITERATE A2; CHOOSE A2 AND TABULATE.
```

```
L=1
A2=2.1700
M.SQ.DEV.= 0.0009463
```

Table A.1b. Fit Results for MAGLSQ. FT, $N_i=9$, $N_p=30$.

| | |
|---|---|
| 16+ | Decide (L) whether it is desired to iterate $a_2$ in order to tabulate $\Delta_m(a_2) \equiv \sqrt{\Delta^2(a_2)/N_p}$, or choose a particular value of $a_2$ and eventually proceed to MAGTAB. FT to tabulate results of fit. |
| 17 to 19 | Read in $a_2$ data for iteration (if L=0) (top Table A.1b). |
| 20 | Read in $a_2$ to obtain coefficients and tabulate results (L=1) (bottom Table A.1b). |
| 21 to 30 | Find $B_{mj}$ coefficients (eliminating roundoff). |
| 30+ to 71 | Solve array for $a_j$ ($c_j$ in program) |
| 71+ to 76+ | Calculate mean square deviation $\Delta(a_2)$ and display depending on L value. |
| 77 | Proceed to MAGTAB. FT (only for L=1) |

MAGTAB. FT is listed in Fig.A.4, with output in Table A.2.

| Statement | Description |
|---|---|
| 78- to 89 | Calculate and tabulate $a_j$ and $g_j$ (top Table A.2). |
| 89+ to 95+ | Calculate and tabulate h(y) and R(y) (bottom Table A.2. First three columns are input data, Table A.1a. Fourth column is the calculated value of h(y), and fifth is $h_j$-h(y). Last column gives R(y). Final operation in program returns to MAGLSQ. FT for further fitting. |

A.6  Conclusions

As shown above, for the particular h(y) data used an rms difference of only .0009 can be obtained with nine coefficients. This is quite small compared to the accuracy with which h(y) can be measured. For four coefficients the result was .0073 and for seven it was .0019. Much was gained going from 4 to 7, but little thereafter. The $N_i = 9$ fit is better than the measurement accuracy.

The h(y) fit is definitely sufficiently accurate to justify its use for the h(y) data used. The $g_j$ coefficients could be employed directly in (A.18) (with K=$a_2$) to find R(y). Eqs. (A.12), (A.13), (A.15) and (A.16) then yield $\epsilon_o$, $x_o$ and x(y) for arbitrary $\epsilon_i$. The only limitation on $\epsilon_i$ is that it be sufficiently small to justify the assumption that h depends only on y.

```
C          MAGTAB.FT: TABULATE FIT RESULTS FROM MAGLSQ. 1/9/78.
           COMMON NPT,Y,H,NP,NI,JM,C,P
           DIMENSION C(9),H(30),Y(30),P(30,16),G(9)
C          SET C(J+1)=C(J), SO C(J)=A(J). TAB. COEFF'S C(J) AND G(J).
           DO 78 J=1,JM
   78      C(NI+1-J)=C(NI-J)
           C(1)=1.
           DO 88 J=1,NI
           I=J-2
           Z=1.
           IF(I)80,80,79
   79      DO 80 K=1,1
           Z=Z*(FLOAT(K)+1.)
   80      CONTINUE
           G(J)=Z
           X=0.
           DO 86 JS=J,NI
           I=JS-2
           Z=1.
           IF(I)82,82,81
   81      DO 82 K=1,I
           Z=Z*(FLOAT(K)+1.)
   82      CONTINUE
           X=X+Z*C(JS)/C(2)**(JS-J)
   86      CONTINUE
           G(J)=X/G(J)
   88      CONTINUE
           WRITE(1,110)
           DO 89 J=1,NI
   89      WRITE(1,106)J,C(J),G(J)
C          COEFFICIENTS TABULATED.
C          TAB. J,Y(J),H(J)ACTUAL,H(J)CALC,DIFF, AND R(Y).
           BM=0.
           WRITE(1,107)
           DO 95 J=1,NPT
           X=1.
           Z=G(1)
           DO 90 K=2,NI
           D=P(J,K-1)
           X=X+D*C(K)
   90      Z=Z+D*G(K)
           D=0
           Q=C(2)*Y(J)
           IF(Q-86.)93,93,94
   93      D=EXP(-Q)
   94      X=X*D
           Z=D*Z/C(2)
           D=H(J)-X
           BM=BM+D**2
   95      WRITE(1,108)J,Y(J),H(J),X,D,Z
           BM=SQRT(BM/FLOAT(NPT))
           Z=G(1)/C(2)
           WRITE(1,109)BM,Z
           CALL CHAIN('MAGLSQ')
  106      FORMAT(I3,2(2X,E14.6))
  107      FORMAT(///' J    Y      HACT     HCALC     DIFF      R(Y)')
  108      FORMAT(I3,2X,F5.2,3(2X,F7.4),2X,F8.5)
  109      FORMAT(/'RMS DIFF ALL PTS='F9.6,'     R(0)='F8.5,////)
  110      FORMAT(///' J        A(J)           G(J)')
           END
```

Fig.A.4. MAGTAB.FT Listing

| J | A(J) | G(J) |
|---|------|------|
| 1 | 0.100000E+01 | 0.255593E+01 |
| 2 | 0.217000E+01 | 0.337636E+01 |
| 3 | -0.602658E+01 | 0.130891E+01 |
| 4 | 0.353369E+02 | 0.530600E+01 |
| 5 | -0.456640E+02 | -0.162918E+02 |
| 6 | 0.258635E+02 | 0.127476E+02 |
| 7 | -0.748371E+01 | -0.474359E+01 |
| 8 | 0.108736E+01 | 0.849436E+00 |
| 9 | -0.645356E-01 | -0.645356E-01 |

| J | Y | HACT | HCALC | DIFF | R(Y) |
|---|-----|--------|--------|---------|----------|
| 1 | 0.50 | 0.9600 | 0.9600 | 0.0000 | 0.70803 |
| 2 | 1.00 | 0.7100 | 0.7101 | -0.0001 | 0.26541 |
| 3 | 1.50 | 0.2650 | 0.2648 | 0.0002 | 0.02889 |
| 4 | 2.00 | 0.0600 | 0.0605 | -0.0005 | -0.04288 |
| 5 | 2.50 | 0.0055 | 0.0044 | 0.0011 | -0.05594 |
| 6 | 3.00 | -0.0130 | -0.0113 | -0.0017 | -0.05352 |
| 7 | 3.50 | -0.0155 | -0.0166 | 0.0011 | -0.04628 |
| 8 | 4.00 | -0.0160 | -0.0167 | 0.0007 | -0.03780 |
| 9 | 4.50 | -0.0155 | -0.0146 | -0.0009 | -0.02992 |
| 10 | 5.00 | -0.0130 | -0.0122 | -0.0008 | -0.02322 |
| 11 | 5.50 | -0.0100 | -0.0102 | 0.0002 | -0.01762 |
| 12 | 6.00 | -0.0080 | -0.0084 | 0.0004 | -0.01296 |
| 13 | 6.50 | -0.0060 | -0.0067 | 0.0007 | -0.00918 |
| 14 | 7.00 | -0.0045 | -0.0051 | 0.0006 | -0.00624 |
| 15 | 7.50 | -0.0035 | -0.0037 | 0.0002 | -0.00406 |
| 16 | 8.00 | -0.0030 | -0.0025 | -0.0005 | -0.00254 |
| 17 | 8.50 | -0.0025 | -0.0016 | -0.0009 | -0.00153 |
| 18 | 9.00 | -0.0020 | -0.0010 | -0.0010 | -0.00089 |
| 19 | 9.50 | -0.0018 | -0.0006 | -0.0012 | -0.00050 |
| 20 | 10.00 | -0.0017 | -0.0003 | -0.0014 | -0.00028 |
| 21 | 10.50 | -0.0016 | -0.0002 | -0.0014 | -0.00015 |
| 22 | 11.00 | -0.0015 | -0.0001 | -0.0014 | -0.00008 |
| 23 | 11.50 | -0.0014 | -0.0001 | -0.0013 | -0.00004 |
| 24 | 12.00 | -0.0013 | -0.0000 | -0.0013 | -0.00002 |
| 25 | 12.50 | -0.0012 | -0.0000 | -0.0012 | -0.00001 |
| 26 | 13.00 | -0.0011 | -0.0000 | -0.0011 | -0.00000 |
| 27 | 13.50 | -0.0010 | -0.0000 | -0.0010 | -0.00000 |
| 28 | 14.00 | -0.0009 | -0.0000 | -0.0009 | -0.00000 |
| 29 | 14.50 | -0.0008 | -0.0000 | -0.0008 | -0.00000 |
| 30 | 15.00 | -0.0007 | -0.0000 | -0.0007 | -0.00000 |

RMS DIFF ALL PTS= 0.000946          R(0)= 1.17785

Table A.2. Tabulation by MAGTAB. FT, $N_i$=9, $N_p$=30.